Available on CMS information server

CMS NOTE 2004/021

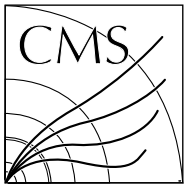

The Compact Muon Solenoid Experiment

CMS Note

Mailing address: CMS CERN, CH-1211 GENEVA 23, Switzerland

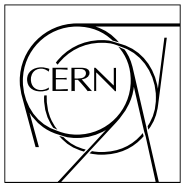

8 October 2004

Validation of Geant4 Physics Using the CMS HCAL Test Beam 2002 Experiment

V. Daniel Elvira

Fermilab, Batavia IL, USA

Abstract

High energy physics measurements relay to a great extent on the accuracy of physics generators and detector simulations. The size of systematic uncertainties associated with particle discoveries, mass, or cross section measurements is tightly associated with how accurately the simulations describe the actual performance of the detector in measuring physics objects. Physics validation studies of Geant4 using physics lists LHEP-3.6 and QGSP-2.7, and based on HCAL test beam taken in 2002, are presented in this note. The pion energy resolution and response linearity as a function of incident energy derived from the simulations are in good agreement with the data measurement within the large systematics uncertainties in the latter. Below 30 GeV, the uncertainties in the data are too large to provide information about deviations of the Monte Carlo model with respect to the data measurements. Transverse and longitudinal shower profiles are also studied in the Monte Carlo, but no data were analyzed. In particular, longitudial segmentation was anavailable in the Test Beam 2002 read out.

1 Introduction

High energy physics experiments depend critically on the accuracy of physics generators and detector simulations. Simulated data events are used for detector design optimization, calibration, object identification, and physics analysis. The size of systematic uncertainties associated with particle discoveries, mass, or cross section measurements is tightly associated with how accurately the simulations describe the actual performance of the detector in measuring electrons, photons, and hadrons. It is imperative, for the success of a HEP experiment, to understand and tune the physics of the simulation tool to agree with the data measurements. With this aim, test beam experiments are conducted which consist of prototypes of the real detectors. In the case of the calorimeter systems, variables such us response, resolution, and shower shapes for pions and electrons of different energies are investigated.

The CMS Collaboration developed the Object oriented Simulation for Cms Analysis and Reconstruction [1] (OSCAR) framework, based on the Geant4 tool kit [2], to describe the detector geometry and the passage of particles through the detector material. Geant4 uses either parametric (LHEP) or microscopic (QGSP) physics models to simulate the particle showers arising from the interaction of particles with matter. For the studies presented in this note, the software package OSCAR_2.4.5 is used, based on GEANT_4.5.2, with LHEP_3.6 and QGSP_2.7 physics lists or models.

The 2002 test beam experiment is described in the next section of this note, while the third section is dedicated to the detector geometry as implemented in OSCAR-GEANT4. A fourth section on results is followed by the conclusions and a discussion on how the simulation accuracy may affect physics results in the CMS experiment.

2 The 2002 HCAL Test Beam Experiment

The 2002 HCAL test beam experiment was a small scale detector setup designed to study the performance of the CMS hadronic calorimeters, described in Ref. [3]. The detector was exposed to beams of π^- (20, 30, 50, 100, 300 GeV), electrons (20, 30, 50, 100 GeV), and muons (225 GeV) over a large energy range. More than 100 million events were read out with at 29.6 ns period, slightly longer than the 25 ns planned for CMS. A total of 144 Hadronic Barrel (HB) channels (two wedges) and 16 Outer Hadronic (HO) channels were tested in a detector configuration which included an aluminum slab, representing the solenoid material, and a mock-up of the electromagnetic calorimeter (ECAL).

2.1 Detector Configuration

A picture of the experimental apparatus is shown in Figure 1. The beam is fixed to the laboratory frame, and a moving table (yellow) is used to change the relative direction of the beam with respect to the detector. This allows the beam to test the different HB towers as a function of ϕ and η. The beam line is equipped with two wire chambers and two scintillator tiles to trigger the events and monitor the beam position. The detector includes a mock-up of the ECAL, consisting of an aluminum box which contains a 7X7 $PbWO_4$ crystal matrix. The crystals are $23\times2.2\times2.2$ cm^3 prototypes with a slightly smaller transverse section upstream than downstream. The box may be translated and rotated for the beam to run along any of the 49 crystals. The ECAL box is followed by two HB wedges positioned together as in the real CMS setup. An aluminum slab accounts for the solenoid material and precedes the outer hadronic calorimeter. The HO consists of two layers of scintillators surrounding an iron block, followed by an iron plate acting as a tail catcher. The inner layer consists of only one panel (Ring 0 covering the central η region), and the outer layer of three panel (Rings 0, 1, 2 covering a larger η range). For the HB and HO, the light from the scintillators is transported to the Hybrid Photo Diodes (HPD) through clear fibers. The signal is then processed by the Charge Integration Electronics (QIE) which gives a short output pulse.

3 OSCAR-GEANT4 Simulation of HCAL Test Beam 2002

The OSCAR-GEANT4 based simulation package of the HCAL Test Beam 2002 (TB02) is called `HcalTB02`. The geometry, beam, and calibration details are described next.

3.1 Geometry

The geometry of the Test Beam 2002 HCAL setup was divided into four sub-system units as described in the previous section: the beam line (BL), the ECAL box (ECAL), the HB wedge, and the HO. Originally, the geometry code was developed using GEANT4 classes under OSCAR_1.4.0 (and older versions). This geometry was later

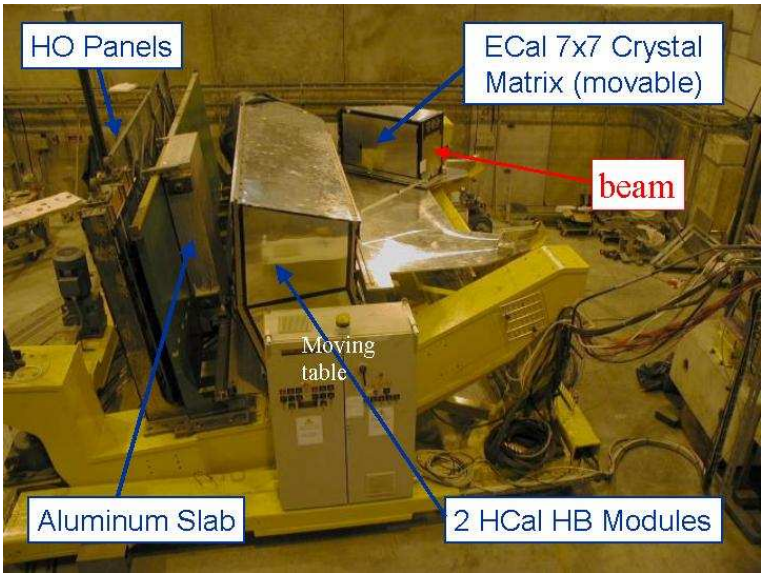

Figure 1: Setup for the 2002 HCAL test beam experiment.

translated to XML format to comply with the OSCAR_2 requirements. The main geometry file is `configuration.xml`, which includes a list of files:

```
TestBeamHCal02.xml
HcalTB02BeamLine.xml
HcalTB02xtalsLogLU.xml
HcalBarrel.xml
HadronOuter.xml
xtalsens.xml
hcalsens.xml
materials.xml
rotations.xml
AllProdCuts.xml
```

`TestBeamHCal02.xml` describes the "world" volume containing the four subsystems: beam line (`HcalTB02BeamLine.xml`), ECAL box (`HcalTB02xtalsLogLU.xml`), HB (`HcalBarrel.xml`), and HO (`HadronOuter.xml`). The sensitive volumes, like the scintillators in the HB-HO and the crystals in the ECAL box, are declared in `hcalsens.xml` and `xtalsens.xml` respectively. Detector materials and rotation matrices used in volume placing are defined in `materials.xml` and `rotations.xml`. `AllProdCuts.xml` contains the cuts in range for production of secondary particles.

By default, the BL and the ECAL subsystems are aligned along the $\hat{x}$ direction, perpendicular to what would be the beam direction in CMS, $\hat{z}$. The HB wedges are placed along the $\hat{x}$ direction with the inner face next to the end of the ECAL and the outer face followed by the HO. The sketch in Fig. 2 contains the elements of the BL system: two wire chambers for tracking and four trigger scintillators, as well as their relative distance. The "pivot" is the center of rotation for the ECAL which may be translated and rotated to point to a particular HB tower. The BL must also translate and rotate to follow a change in the test beam direction. The HB and the HO are fixed in space. Figure 3 displays an OpenGL [6] image of the BL as simulated in `HcalTB02`.

The sketch in Fig. 4 shows the ECAL box geometry detail as implemented in `HcalTB02`. The 7X7 array of crystals is encased in a 2 mm thick aluminum box. They are preceeded by a 2.3 cm block of plexiglass plus 5 cm more to account for the material of the light guides connecting the crystals to the photo-multipliers. An 8 cm aluminum block behind the ECAL box represents the material between the crystals and the HB in the actual CMS setup. The fixation point marks the position of the HB inner face. The crystals are 23 cm long and have a projective geometry in the radial direction, with a maximum section of 2.2x2.2 cm^2. Figures 5- 6 display OpenGL images of the ECAL box system as simulated in `HcalTB02`.

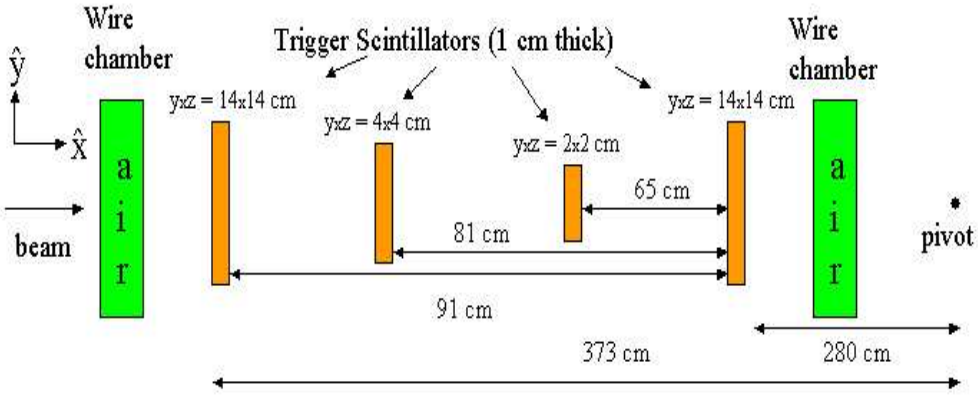

Figure 2: Sketch of the beam line (BL) system.

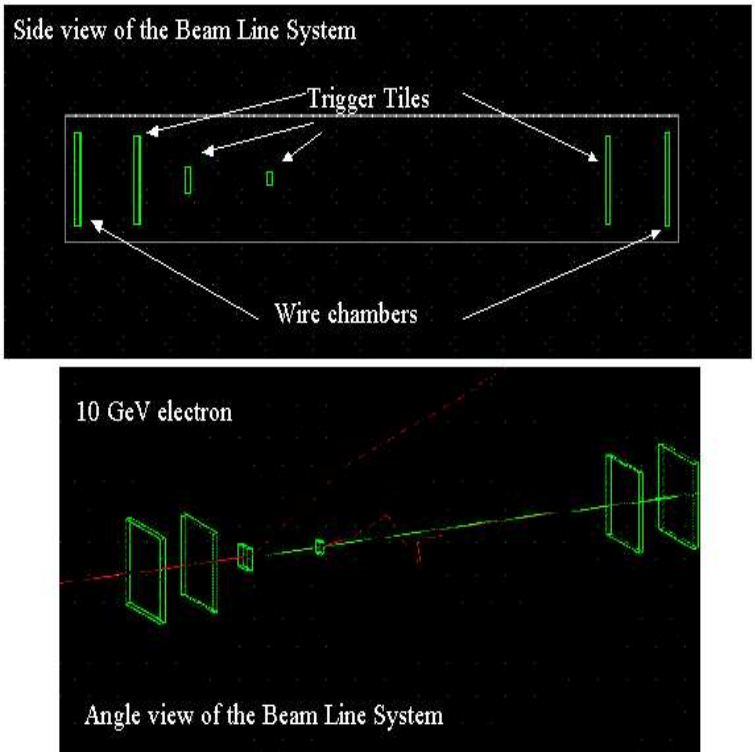

Figure 3: OpenGL image of the beam line as simulated in `HcalTB02`.

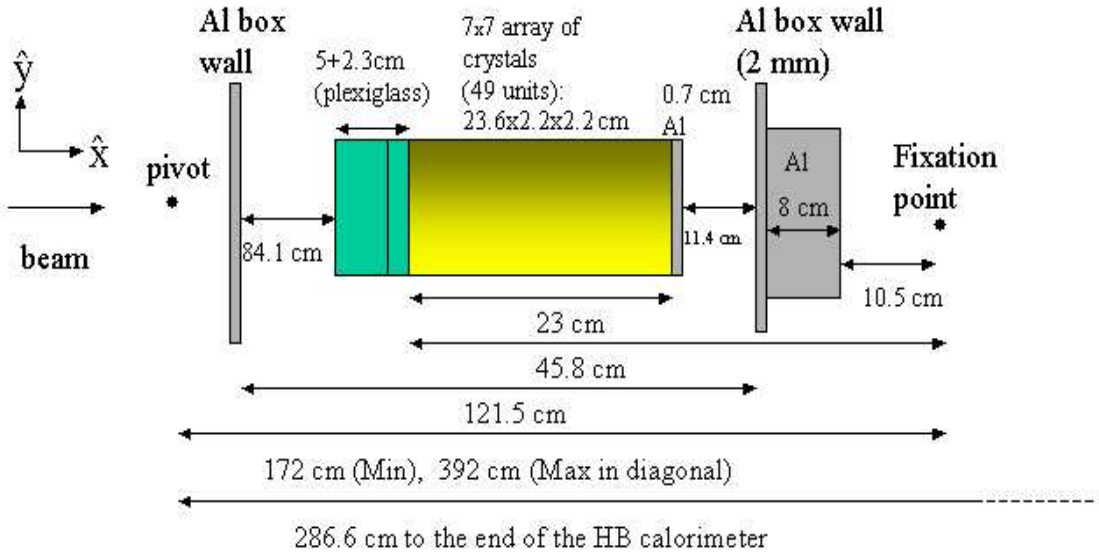

Figure 4: Sketch of the ECAL box (ECAL) system.

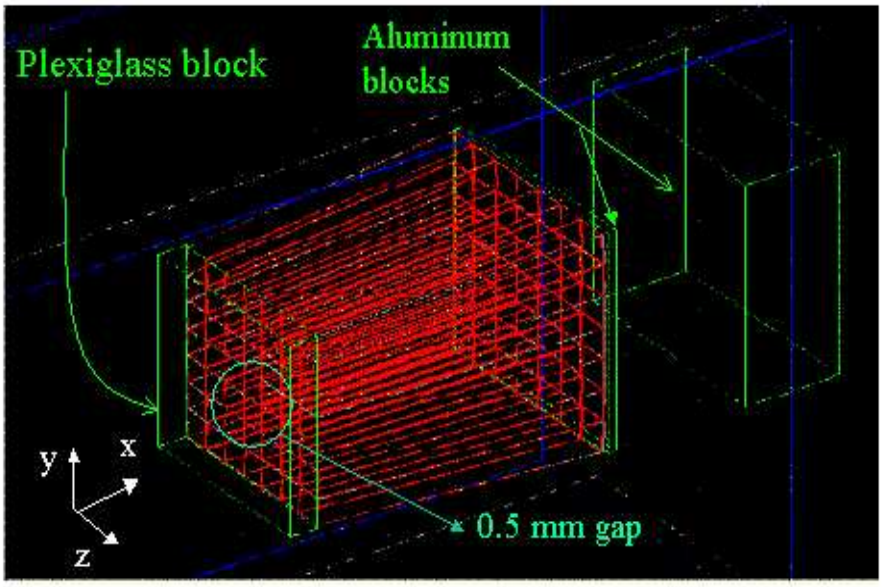

Figure 5: OpenGL image of the ECAL box as simulated in `HcalTB02`.

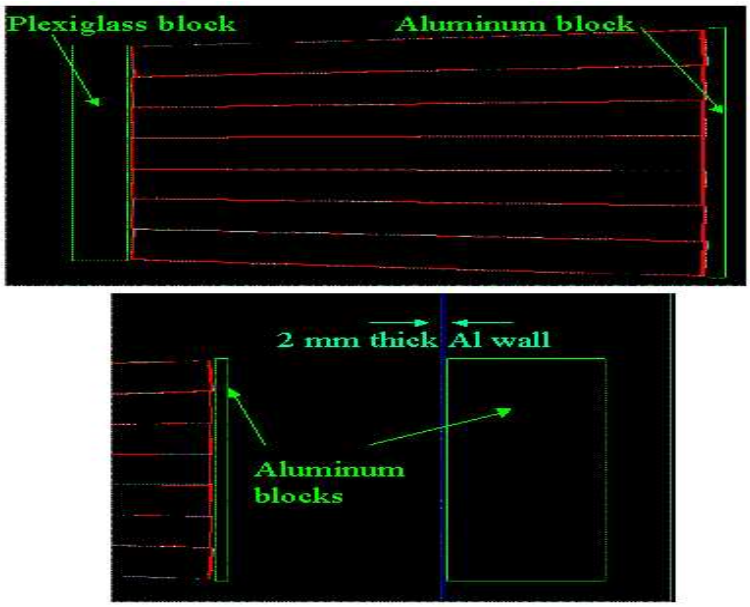

Figure 6: OpenGL detail image the ECAL box (ECAL) as simulated in `HcalTB02`.

The two HB wedges used in the TB02 experiment are production modules, which will be part of the actual CMS detector. The shape and thickness of the brass layers 2-16 in the simulation follows those of the actual wedge, 6 cm for layers 2-10 and 6.6 cm for layers 11-16. The steel layers, one and 17, are 7.45 cm and 8.9 cm thick respectively. In the CMS detector, the first layer of each HB wedge supports an ECAL super-module, which fits in the dent machined into the stainless steel plate, shown in Fig. 7 as the "air" volume. In the test beam experiment and simulation, this volume is actually empty space. In the CMS experiment, the coupling section of the ECAL outermost steel plate fits in the first HB steel layer, and is considered part of the HB in the CMS simulation. Figure 8 displays an OpenGL image of the HB as simulated in `HcalTB02`. The thickness of the scintillation tiles, shown in blue in Fig. 8, is 0.4 cm in layers 2-16, and 0.8 cm in layers one and 17.

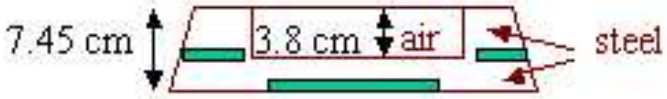

Figure 7: Geometry detail of layer one of the HB.

Figure 8 also illustrates the HO geometry details included in the simulation. The aluminum slab, 310 mm thick, accounts for the solenoid material and is followed by the 100 mm iron yoke. The iron tail catcher, 195 mm thick, lies in between the two scintillator layers and covers only the Ring 0 region.

3.2 Readout Signal and Electronic Noise

As discussed in Ref. [3], the total noise for the fully integrated signal (4 time slices) is 520 MeV. The noise contribution in a channel was, therefore, included in the simulation by adding a Gaussian term with a σ=520 GeV centered about the total energy deposited in a tower: $E_{tower} \times (1 + \mathrm{Random} \times \sigma)$.

3.3 Beam and Run Conditions

The TB02 experiment included an energy scan for π^- onto the BL-ECAL-HB-HO configuration: 20, 30, 50, 100, 300 GeV. These data were used to measure pion energy resolution and response in the 20-300 GeV energy range. In order to validate the physics of GEANT4, simulation samples were generated in the same range: 10000, 8000, 5000, 3000, and 2000 π^- events at 20, 30, 50, 100, and 300 GeV. Although the TB02 experiment did not have any longitudinal readout segmentation, but only one measurement per tower, the longitudinal and transverse profiles of the pion showers were simulated using the HB-HO and HB configurations, respectively. Data for comparison

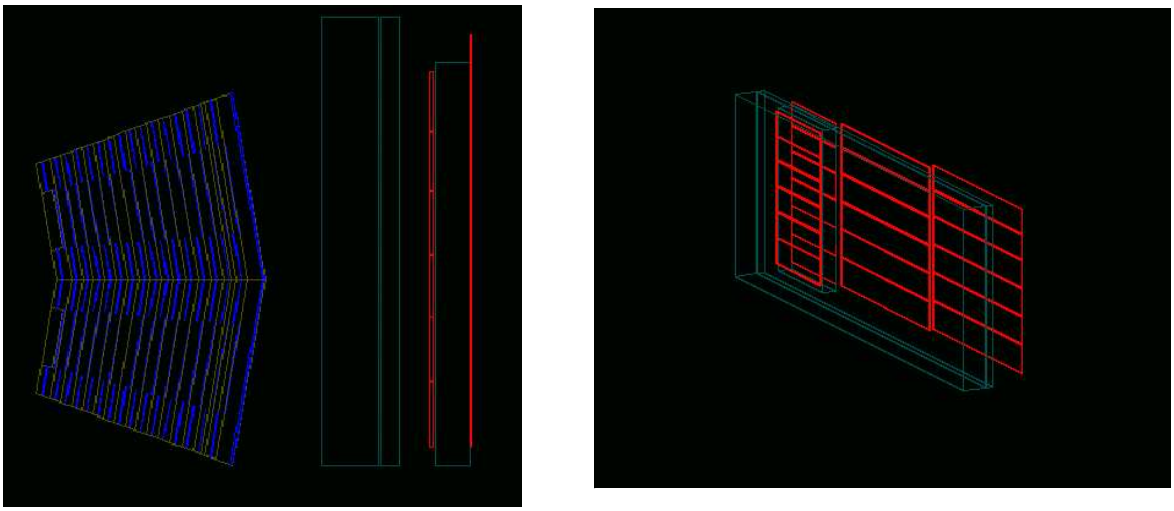

Figure 8: OpenGL image of the HB and the HO (angle view) as simulated in `HcalTB02`.

will be available from the upcoming test beam 2004 (TB04) experiment. Calibration samples were also generated to adjust the ECAL and HB energy scale: 100 GeV electrons onto the ECAL and 50 GeV pions onto the HB only.

As in the TB02 experiment, the pion beam was generated in the direction of the (η#,ϕ#)=(9,4) tower, and the BL-ECAL system translated and rotated so that the beam passed through the BL geometric center and the central crystal of the 7X7 matrix. The position of tower (9,4) within the HB TB02 configuration is illustrated in Fig. 9. The sketch in Fig. 10 displays details on the beam angle and relative position between the different subsystems.

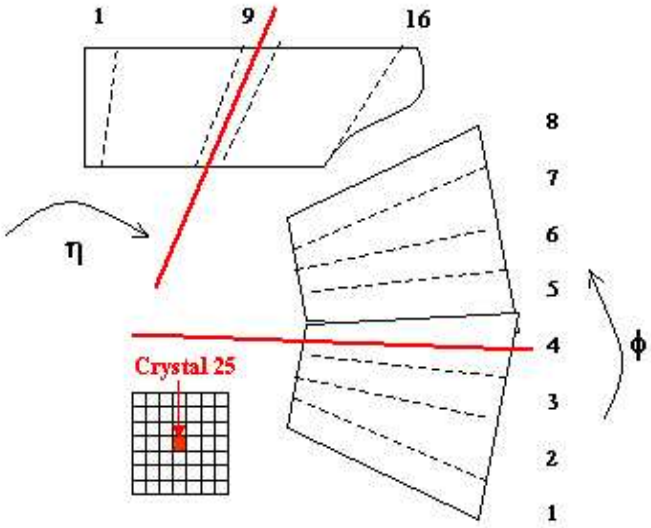

Figure 9: Position of tower (η#,ϕ#)=(9,4) within the HB TB02 configuration.

Production cuts in range for secondary particles are GEANT4 user defined parameters which control the shower development. In `AllProdCuts.xml`, these cuts were set to 1 mm for both electrons and positrons and 10 mm for photons, except in the ECAL where the later cut was set to 1 mm. Figure 11 illustrates on the shower development of a 10 GeV electron in the ECAL box, while Fig. 12 displays a 100 GeV pion shower in the HB.

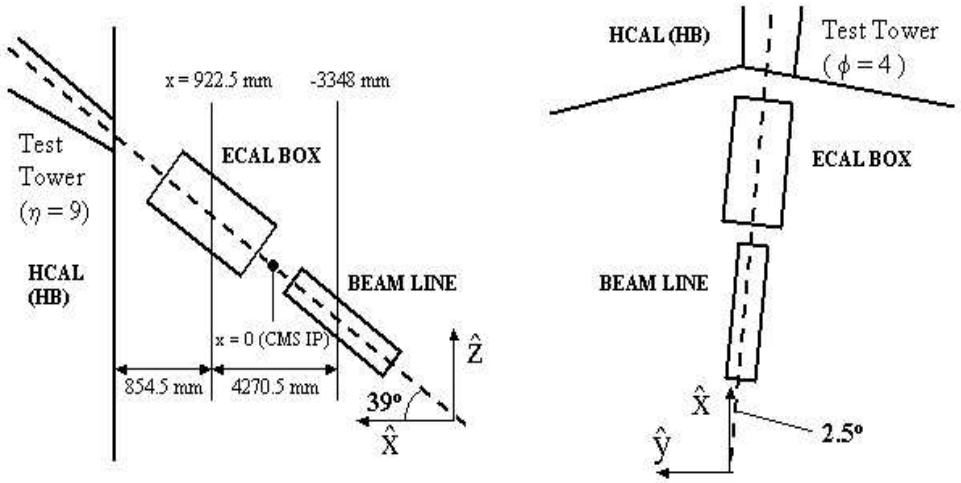

Figure 10: Sketch of the beam direction and relative positions between the different TB02 subsystems.

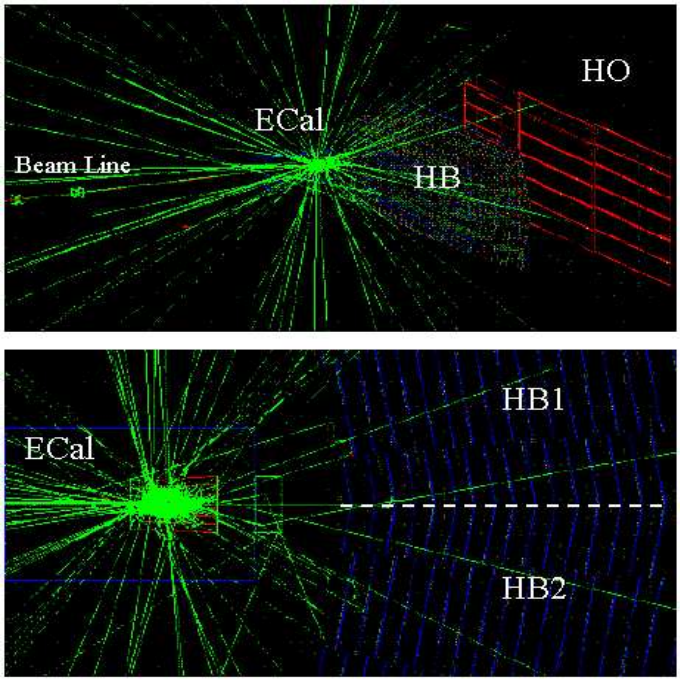

Figure 11: Shower development of a 10 GeV electron in the ECAL box.

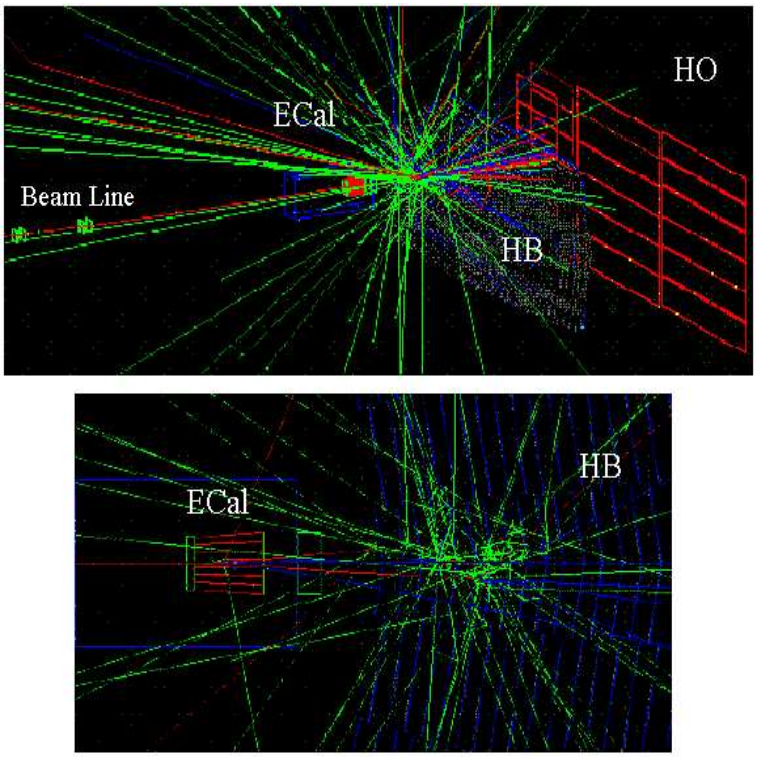

Figure 12: Shower development of a 100 GeV pion in th

3.4 Calibration

The energy calibration of the ECAL box and the HB in the simulation follows closely that of the actual TB02 experiment. While electrons deposit most of their energy in the ECAL box active material, the $PbWO_4$, pions deposit most of their energy in the HB passive material, the brass or steel. Almost 95% of the electron energy is readout from the crystals in the ECAL but less than 1% of the pion energy is readout from the HB scintillators, since the HB is a sampling calorimeter.

The energy scale of the ECAL box is derived using a 100 GeV electron beam from the ratio between the initial energy E_i^e of the beam and the mean of the distribution of the energy deposited in a 3X3 matrix around the central crystal. The energy scale of the HB was derived in the actual TB02 experiment in several steps. First, a Co^{60} source was used to calibrate the individual scintillator tiles to make the detector uniform. Second, a beam of 100 GeV electrons was directed onto a given HB tower to provide an estimate of the ADC counts to GeV conversion factor. In the third step, a beam of 50 GeV pions were directed to the ECAL-HB configuration. Only those pions which showered late, that is they deposited less than 2 GeV in the crystals, were selected. The calibration factor was extracted as the ratio between the initial pion energy E_i^π and the mean of the sum of the energy depositions in the scintillators associated with a 5X5 tower matrix around the target tower. In the simulation, the HB calibration factor was derived directly from a procedure similar to step three. A beam of 50 GeV pions was directed onto the HB only configuration, avoiding the need to remove the pions which showered early in the ECAL.

Figure 13 contains two plots of the energy distribution in the crystals for a beam of 100 GeV electrons. Both physics lists, LHEP-3.6 and QGSP-2.7 give energy resolutions in excellent agreement with each other. The value σ_E/E(100 GeV)$\sim$0.5 from the simulation is, however, about four times smaller than the measured electron energy resolution, 2.2%, in the TB02 experiment [7]. The simulated value includes the effect of electronic noise estimated in 115 GeV per crystal. The addition of other effects like a $2.3\%/\sqrt{E}$ (photo-statistics), a 0.3% (longitudinal non-uniformity of crystals), and a 0.4% (calibration) produces a minimal effect, and cannot describe the large difference between the measurement and the simulated data. Some possible explanations are the large dependence on temperature, $2\%/^\circ C$, of the crystal response, radiation damage, longitudinal non-uniformity in the prototype crystals used in TB02 larger than that in the design specifications for production crystals. As a test of the effect of this discrepancy on the accuracy of a realistic simulation of the pion energy resolution of the ECAL-HB system, the ECAL energy per crystal was smeared with a random factor following a Gaussian distribution around the mean energy deposition. This additional random term was tuned so that the electron energy resolution simulated

in the range 20-100 GeV agreed with the experimental values: 5% (20 GeV), 3% (50 GeV), 2.2% (100 GeV). The relative degradation in the fractional energy resolution for pions when incorporating the extra smearing to the ECAL energy is 3% (1% absolute) at 20 GeV, and 0.6% (0.06% absolute) at 300 GeV. The calibration factor for the ECAL, derived as explained above, is 1.061.

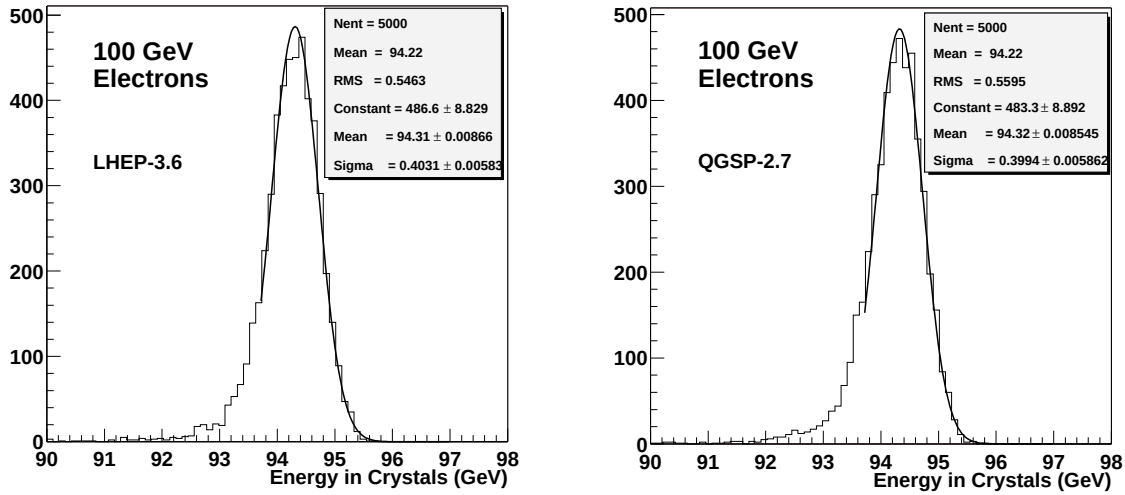

Figure 13: Energy distribution in the crystals for a beam of 100 GeV electrons. Both physics lists, LHEP-3.6 and QGSP-2.7 give an energy response and resolution in excellent agreement with each other.

The energy distributions for 50 GeV pions, using the LHEP-3.6 and QGSP-2.7 physics lists, are displayed in Fig. 14. Since the HB is a sampling calorimeter, only a small fraction, $<1\%$, of the pion energy is deposited in the active medium, the scintillators. The calibration factor for the HB is therefore large, 117.3, and does not depend significantly on the available physics lists.

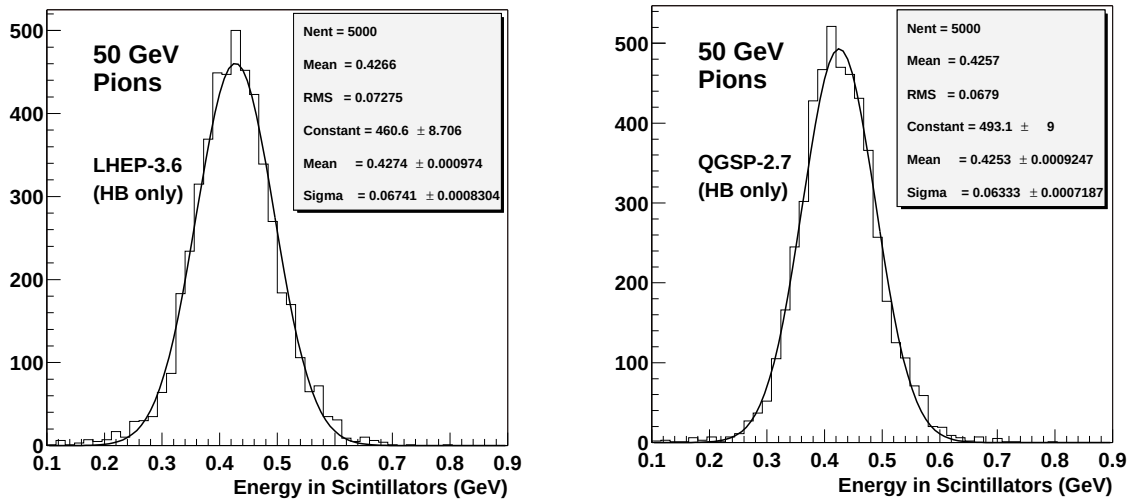

Figure 14: Energy distribution in the scintillators for a beam of 50 GeV pions. The two physics lists, LHEP-3.6 and QGSP-2.7 give very similar energy response and resolution.

4 Simulation Results and Comparison with Test Beam 2002 Data

The variables selected to validate the physics of the simulation against the TB02 measurements are: response and resolution as a function of the energy of the incident pion, transverse or lateral size of the pion shower, as well as its longitudinal shape. A good description of these calorimeter performance variables is essential for a Monte Carlo simulation to serve as a tool in data analysis.

As discussed in Ref. [3], compensation is one of the key physical properties that characterizes a calorimeter. In non-compensating calorimeters, the signal is not linearly proportional to the hadron energy and e/π, the ratio between the response to electrons and pions, is energy dependent. Calibration is typically easier and more accurate for a calorimeter with a linear energy response to hadrons, and departures from this behavior have to be well understood to achieve small calibration uncertainties. The DØ calorimeters [9] are a good example of a hermetic and compensating system, with a e/π <1.05 for E_π >30 GeV and a Gaussian response function. The characteristics of single pion energy distributions in the CMS Barrel Hadronic calorimeter will be discussed in detail in the next section.

Shower shapes are also important variables to validate in a Monte Carlo simulation. The longitudinal development of a hadronic shower determines the amount of energy deposited beyond the calorimeter outer boundaries and the relative weight of the different layers in the total energy calculation. These factors affect the missing transverse energy ($\not\!\!E_T$) calculation and the calibration constants in general. A good Monte Carlo representation of transverse shower profiles is critical for the jet algorithms to behave the same as in data, as well as to understand jet shapes and out-of-cone showering effects. Although the TB02 experiment did not produce data to study shower profiles, results from the simulation are presented in the following sections as a preparation for the TB04 experiment which will include longitudinal readout segmentation.

4.1 Energy Distributions for Pions

Pion energy distributions were studied from simulated pion beams with energies between 20 and 300 GeV showering through the BL-ECAL-HB system, as described in Section 3.3. The initial pion energy was reconstructed from calorimeter information as: $E_{\pi^-} = 1.061 \times E_{ECAL5X5} + 117.3 \times E_{HB5X5}$, where $E_{ECAL5X5}$ is the total energy from depositions in a 5X5 ECAL crystal matrix around the central crystal, and E_{HB5X5} is the total energy from depositions in a 5X5 HB tower matrix about the central tower.

Figures 15 and 16 contain E_{π^-} Monte Carlo distributions for 20, 30, 50, 100, and 300 GeV pion beams, using either the LHEP-3.6 or the QGSP-2.7 physics list. Figures 17 and 18 show the same distributions from a simulation without electronic noise. The high energy non-Gaussian tails in the low energy distributions are a noticeable feature, illustrating on the non-compensating nature of the CMS calorimeters. The CMS HB has a e/h of 1.4-1.5, depending on the $F(\pi^\circ)$ model considered [10], and the BL-ECAL-HB system tested in this simulation is even less compensating. It is interesting to note that the electronic noise masks most of the non-Gaussian nature of the energy distributions for low energy pions, as it is apparent from a comparison of the top two plots of Figs. 15 - 18.

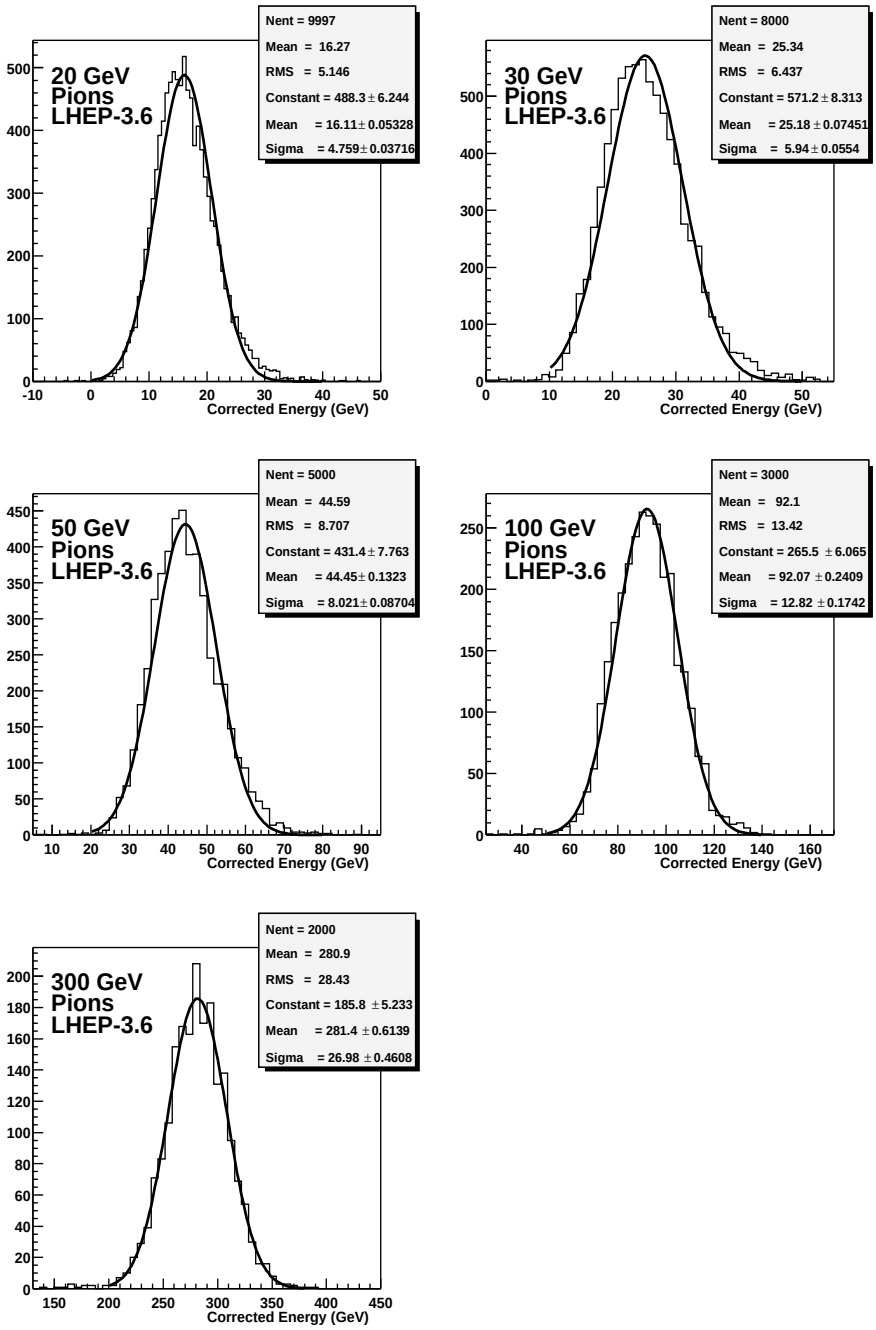

Figure 15: Energy distributions in the Beam Line + ECAL box + Hadronic Barrel configuration for pions, using the LHEP-3.6 physics list. The simulation includes electronic noise.

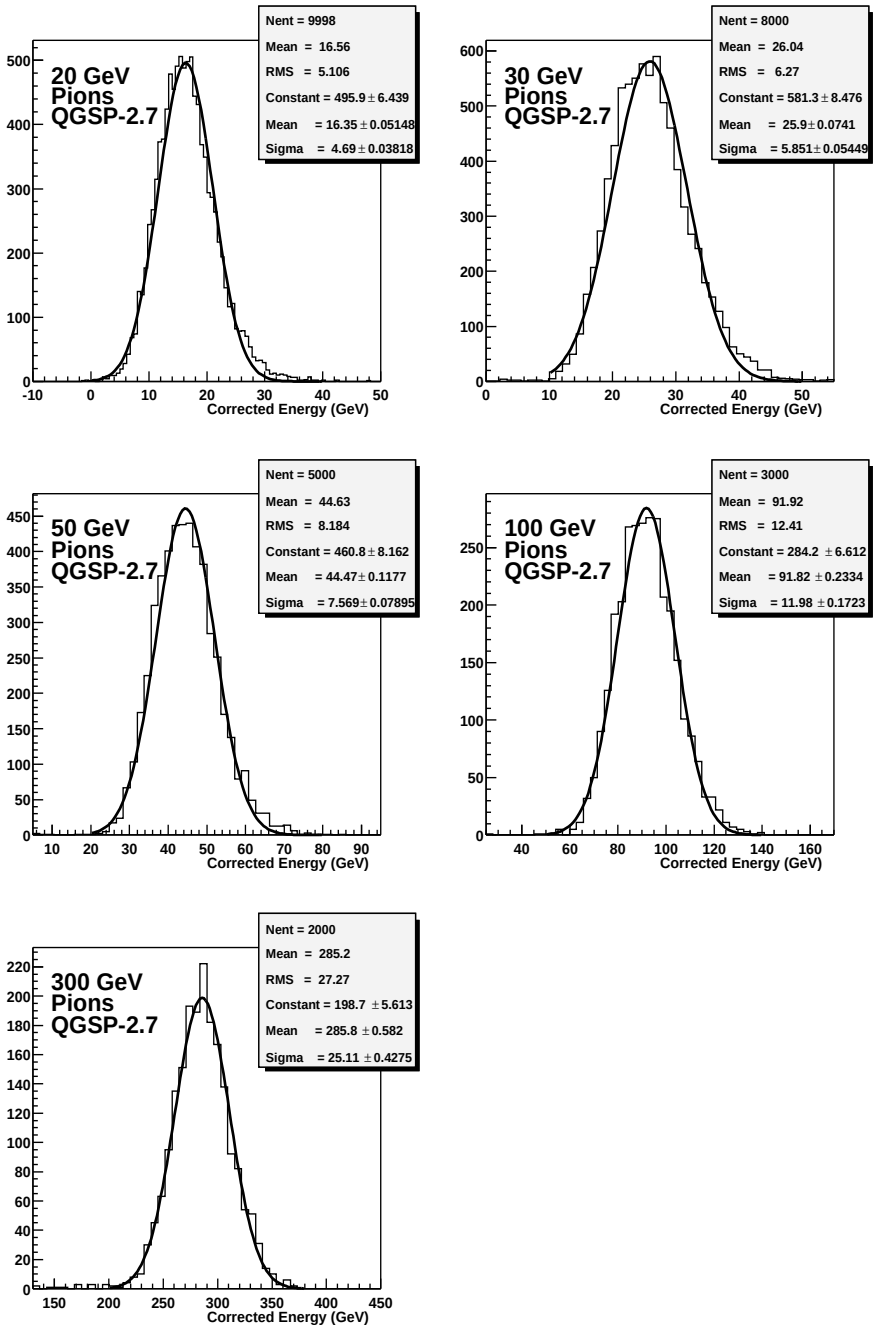

Figure 16: Energy distributions in the Beam Line + ECAL box + Hadronic Barrel configuration for pions, using the QGSP-2.7 physics list. The simulation includes electronic noise.

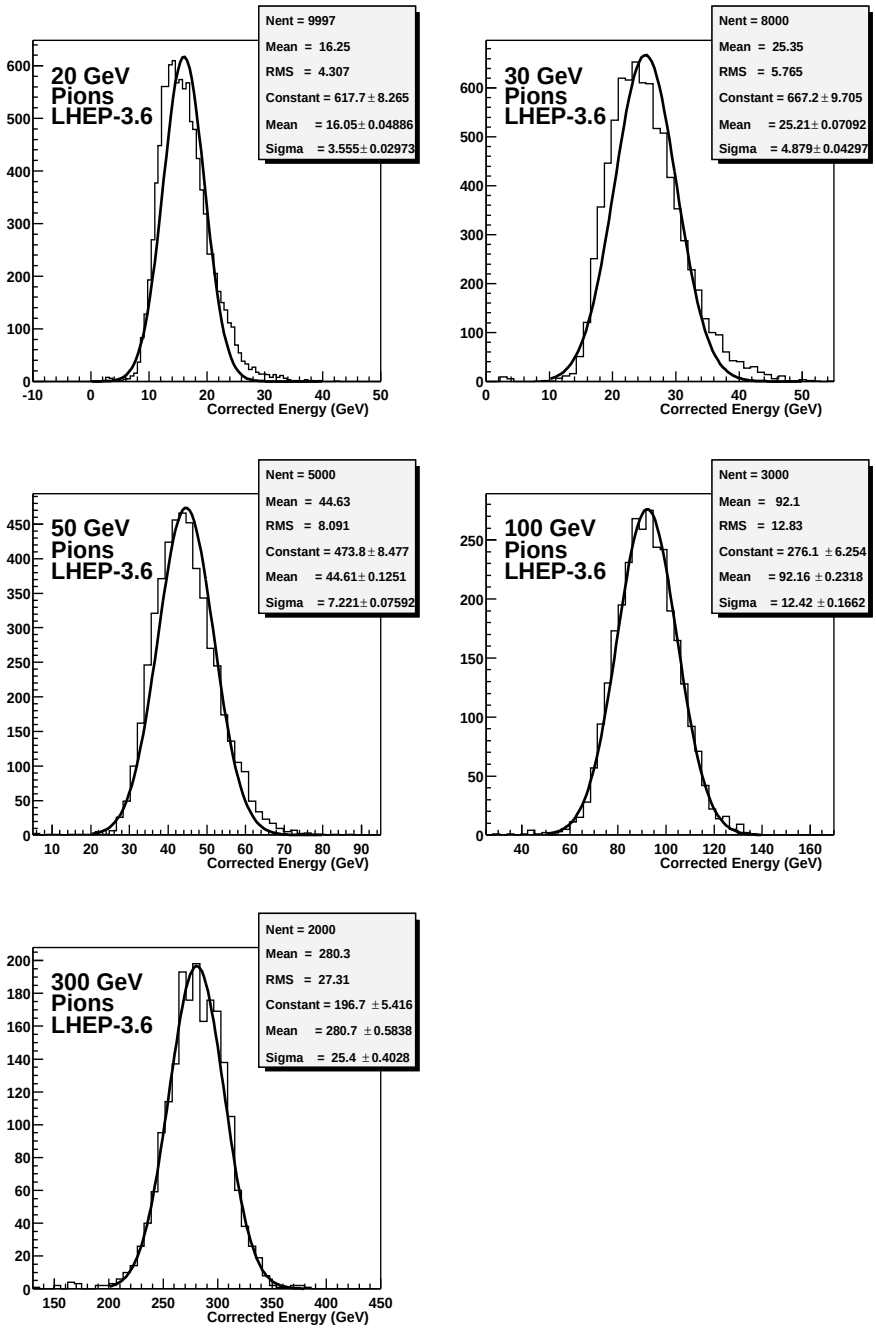

Figure 17: Energy distributions in the Beam Line + ECAL box + Hadronic Barrel configuration for pions, using the LHEP-3.6 physics list. The simulation does not include electronic noise.

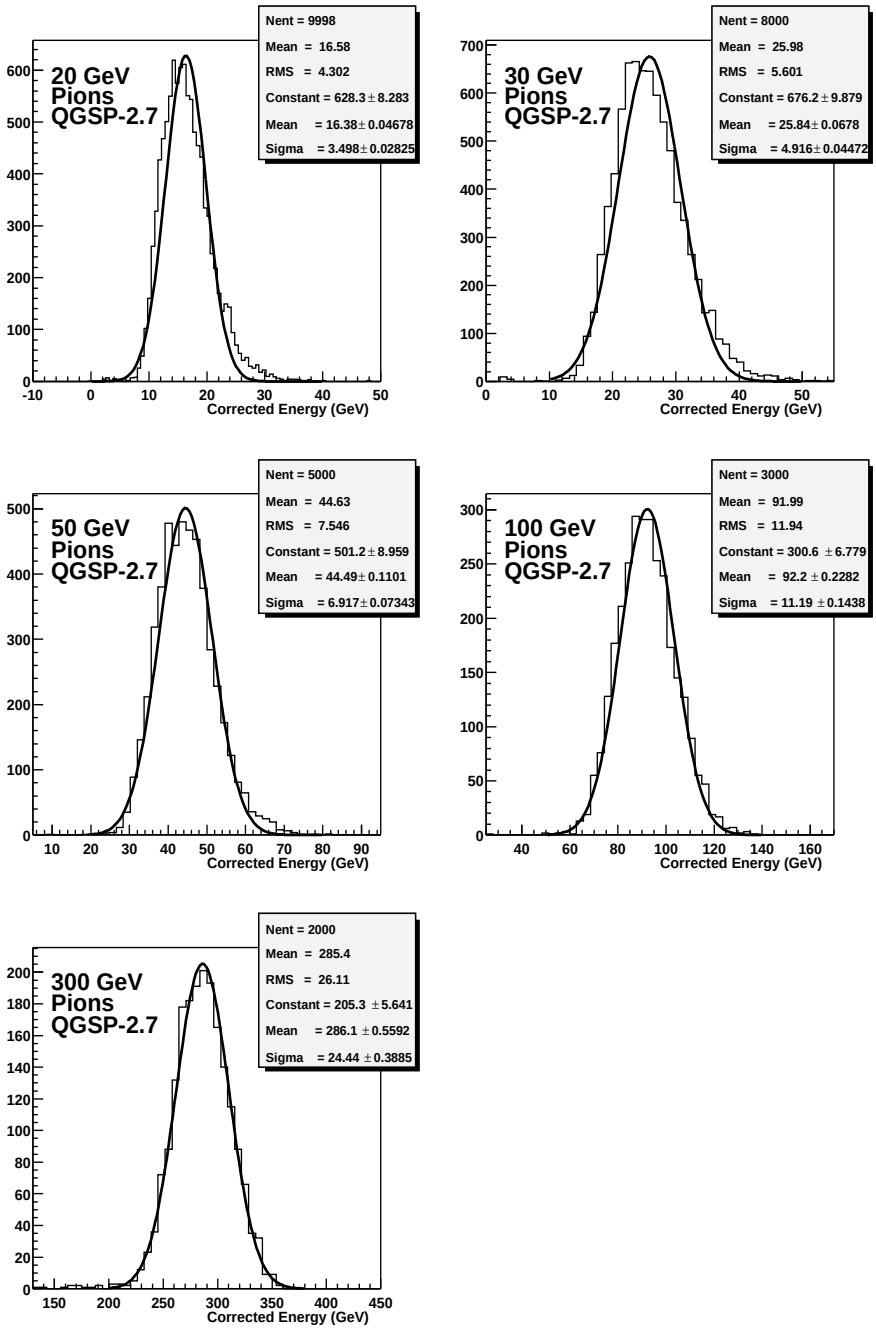

Figure 18: Energy distributions in the Beam Line + ECAL box + Hadronic Barrel configuration for pions, using the QGSP-2.7 physics list. The simulation does not include electronic noise.

4.2 Linearity

Figure 19 shows the response of the BL-ECAL-HB system to π^- as a function of energy calculated as E_{π^-}/E_i, where E_{π^-} is the mean of Gaussian function fit to the energy distributions and E_i is the initial beam energy. The result from the `HcalTB02` simulation, using LHEP-3.6 or QGSP-2.7, with and without electronic noise, is compared with the TB02 data measurement. The vertical bars are the statistical and systematic uncertainties in the data measurement added in quadrature. For comparison, the simulated linearity plots were scaled up by 5% (LHEP) and 3% (QGSP) to approximately match the data at 300 GeV. Within the experimental uncertainties, there is good agreement between the data and the simulation. While the LHEP-3.6 physics list predicts a response growing slightly faster than the measured in data, the one derived from the QGSP-2.7 physics list grows slower. The electronic noise does not affect this measurement significantly. The data measurement and the simulation are easier to compare in Fig. 20, which features the ratio between the results from the simulation and the data. Figure 21 shows response results calculated as Mean/E_i, where Mean is the arithmetic mean of the energy distribution and E_i the initial beam energy. The difference between the two alternate ways of presenting the calorimeter response results are not significant.

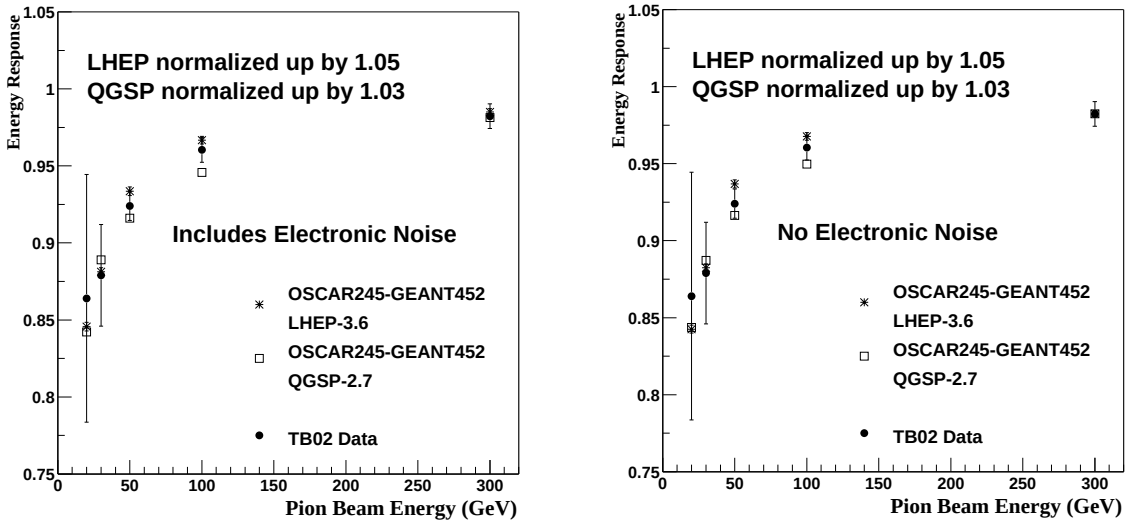

Figure 19: In the Beam Line + ECAL box + HB configuration for pions, comparison between the simulated and measured energy response, E_{π^-}/E_i, using both LHEP-3.6 and QGSP-2.7 physics lists.

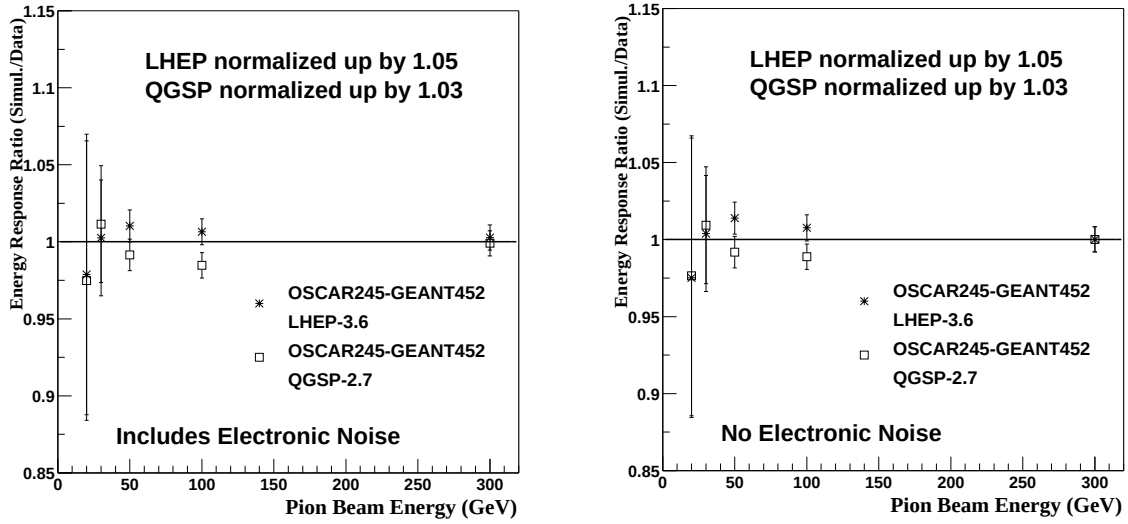

Figure 20: In the Beam Line + ECAL box + HB configuration for pions, ratio between the simulated and measured energy response, E_{π^-}/E_i, using both LHEP-3.6 and QGSP-2.7 physics lists.

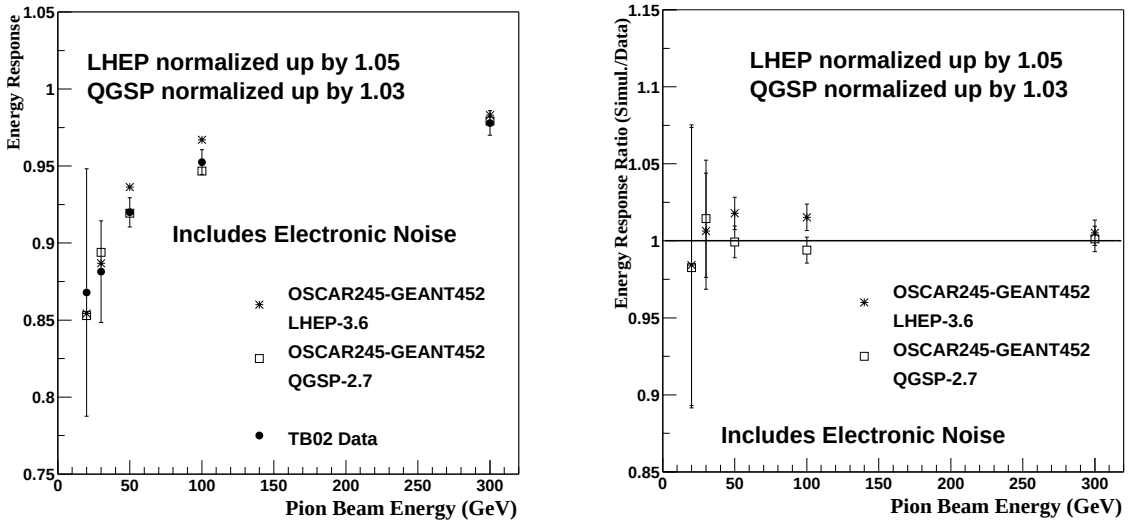

Figure 21: In the Beam Line + ECAL box + HB configuration for pions, comparison between the simulated and measured energy response, Mean$/E_i$, using both LHEP-3.6 and QGSP-2.7 physics lists. The ratio between the simulated and the measured energy resolution is also shown.

4.3 Resolution

Figure 22 shows the resolution of the BL-ECAL-HB system for π^- as a function of energy calculated as σ/E_{π^-}, where E_{π^-} is the mean and σ the square root of the variance of a Gaussian function fit to the energy distributions. The vertical bars are the statistical and systematic uncertainties in the data measurement added in quadrature. The data measurement is in good agreement with the simulation, for the two physics lists tested, given the high correlation of the TB02 measurement uncertainties point-to-point in pion energy. The LHEP-3.6 physics list gives a fractional energy resolution a few percent larger than the QGSP-2.7 list. The data results and Monte Carlo prediction are easier to compare in the ratio plot shown in Fig. 23. The electronic noise contribution to σ_E/E becomes increasingly relevant as the pion beam energy decreases. At 20 GeV, the resolution degrades by a little more than 30% when a realistic electronic noise model is incorporated to the simulation, as it is shown in Fig. 23.

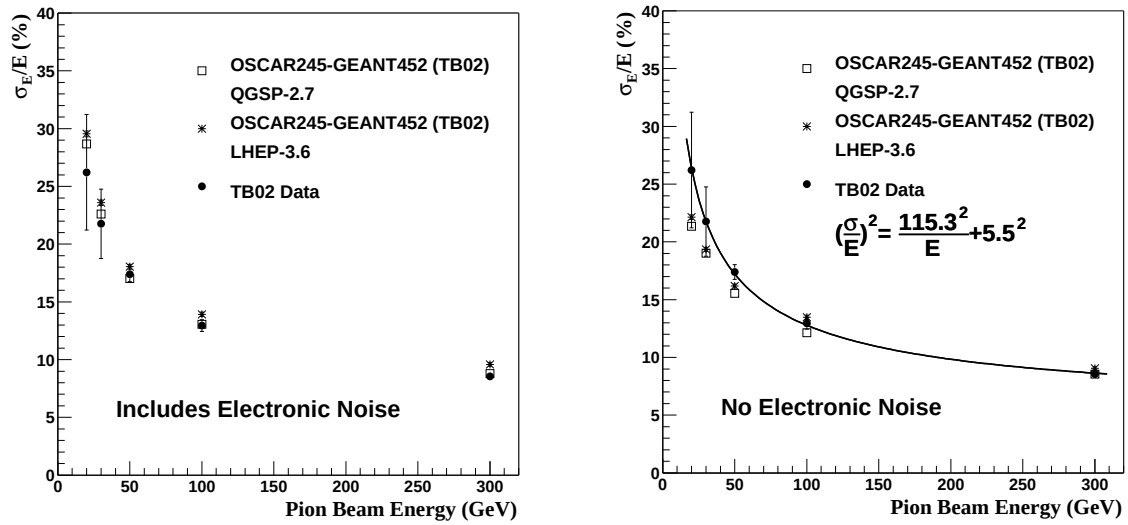

Figure 22: In the Beam Line + ECAL box + HB configuration for pions, comparison between the simulated and measured energy resolutions, σ/E_{π^-}, using both LHEP-3.6 and QGSP-2.7 physics lists.

Figure 24 shows resolution results calculated as RMS/Mean, where Mean is the arithmetic mean of the energy distribution and RMS the root mean square. While the nominal resolution values extracted from Gaussian fits at

high energies, $E_i = 100 - 300$ GeV, are slightly higher than the data measurement, those derived directly from the arithmetic mean and RMS of the distributions are slightly lower than the data. This is a manifestation of the non-Gaussian tails being more prominent in data than in the simulation, probably because of the Monte Carlo predicting shorter showers and therefore a smaller energy leakage effect.

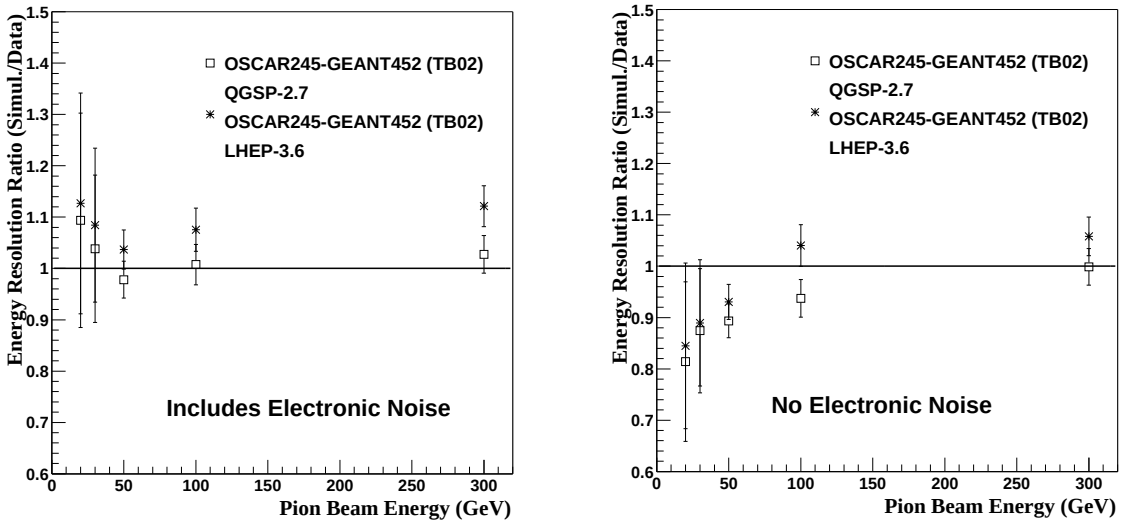

Figure 23: In the Beam Line + ECAL box + HB configuration for pions, ratio between the simulated and measured energy resolutions, σ/E_{π^-}, using both LHEP-3.6 and QGSP-2.7 physics lists.

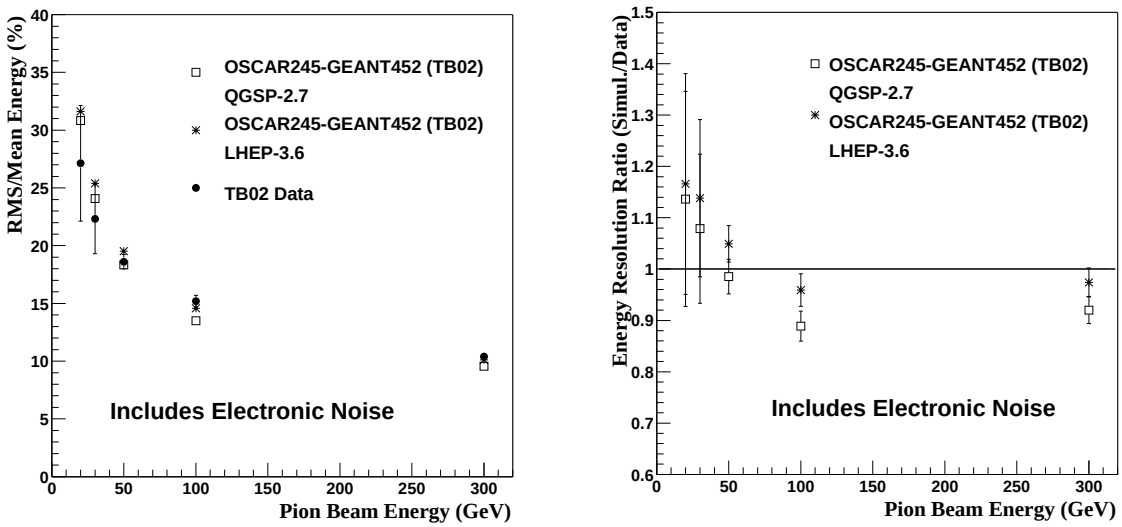

Figure 24: In the Beam Line + ECAL box + HB configuration for pions, comparison between the simulated and measured energy resolutions, RMS/Mean, using both LHEP-3.6 and QGSP-2.7 physics lists. The ratio between the simulated and the measured energy resolution is also shown.

4.4 Transverse Shower Profiles

The transverse profiles of pion showers with energies of 20, 30, 50, 100, and 300 GeV were studied using the HB only configuration. The energy deposited in each HB tower was integrated from the outside to the center of the shower and studied as a function of its distance in η-ϕ space to central tower ($\eta\#$,$\phi\#$)=(9,4): ΔR=$\sqrt{(\eta-\eta_9)^2+(\phi-\phi_4)^2}$, where η_9 and ϕ_4 defines the position of (9,4). Figures 25-29 show the fraction of the shower energy contained in ΔR rings which start at a distance R=0.5 of the center of the shower and grow towards the central tower located at R=0. The ring with outer radius 0.5 and inner radius 0.05 excludes only the central tower and contains 16.78% (18.75%) of the shower energy when using LHEP-3.6 (QGSP-2.7). The distribution follows a step function pattern because it changes as new sets of towers are incorporated to the integral: nearest neighbor towers, next-to-nearest, and so on. Table 1 displays the predicted values for the energy fraction deposited outside the central tower for pions with energies between 20 and 300 GeV. The table also includes the mean and RMS of the distributions, as well as the CMSIM (Geant3) [11] prediction of the energy fraction outside the central tower whenever available [12]. Pion showers predicted by Geant4 are narrower than those predicted by Geant3. The data collected by the upcoming Test Beam 2004 experiment will be critical to validate or tune transverse shower profiles in Geant4.

Table 1: Predicted values for pion transverse energy profiles: mean, RMS, energy fraction deposited outside the central tower for pions with energies between 20 and 300 Gev.

Energy (GeV)	Physics List	Mean	RMS	Energy (%) Fraction
20	LHEP-3.6	0.0300	0.047	18.75
20	QGSP-2.7	0.0272	0.042	16.78
20	CMSIM			21
30	LHEP-3.6	0.0293	0.046	17.85
30	QGSP-2.7	0.0247	0.039	14.40
50	LHEP-3.6	0.0268	0.043	16.00
50	QGSP-2.7	0.0237	0.038	13.56
100	LHEP-3.6	0.0254	0.041	14.68
100	QGSP-2.7	0.0221	0.036	12.02
100	CMSIM			16
300	LHEP-3.6	0.0239	0.039	13.30
300	QGSP-2.7	0.0202	0.033	10.10
300	CMSIM			13

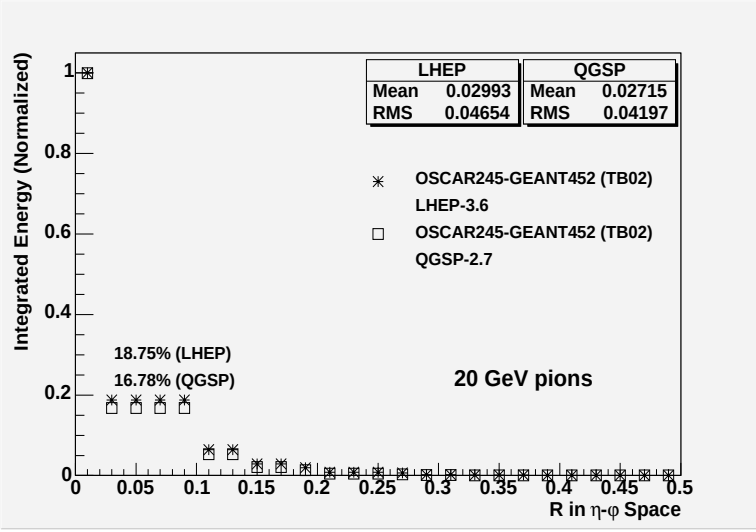

Figure 25: In the HB only configuration for pions, comparison between lateral shower profiles using both LHEP-3.6 and QGSP-2.7 physics lists in the simulation. The percent numbers in the figure refer to the fraction of energy deposited outside the central HB tower ($\eta\#$,$\phi\#$)=(9,4).

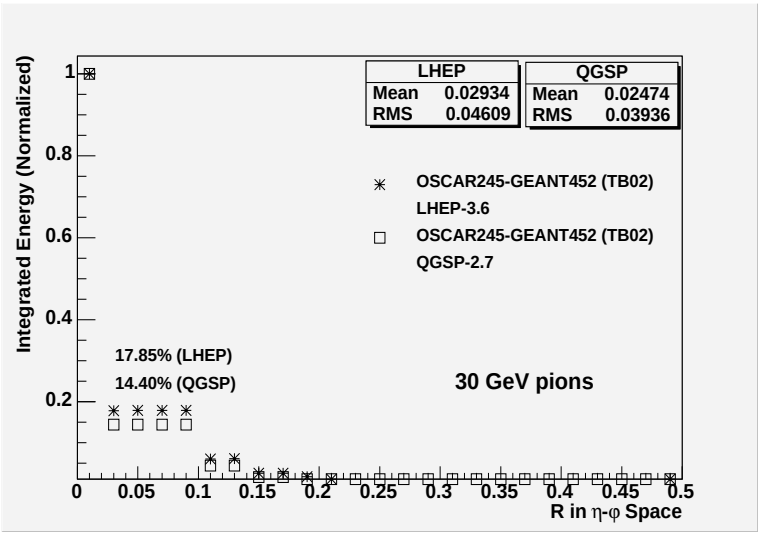

Figure 26: In the HB only configuration for pions, comparison between lateral shower profiles using both LHEP-3.6 and QGSP-2.7 physics lists in the simulation. The percent numbers in the figure refer to the fraction of energy deposited outside the central HB tower ($\eta\#$,$\phi\#$)=(9,4).

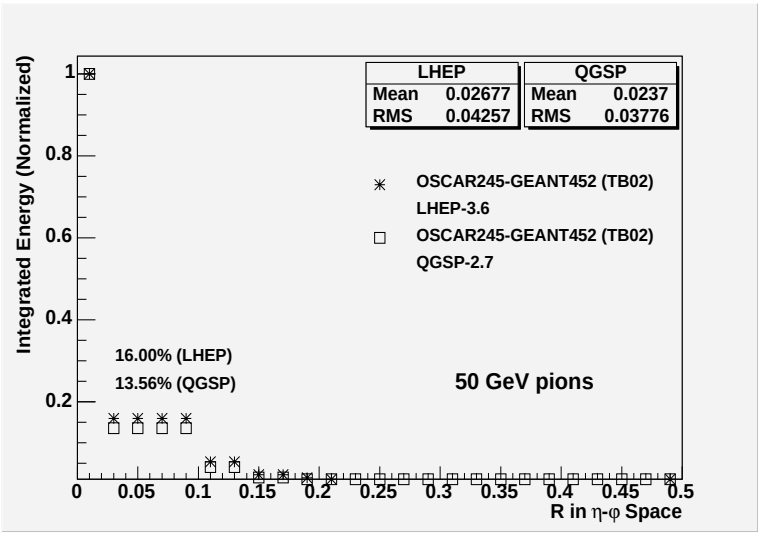

Figure 27: In the HB only configuration for pions, comparison between lateral shower profiles using both LHEP-3.6 and QGSP-2.7 physics lists in the simulation. The percent numbers in the figure refer to the fraction of energy deposited outside the central HB tower ($\eta\#$,$\phi\#$)=(9,4).

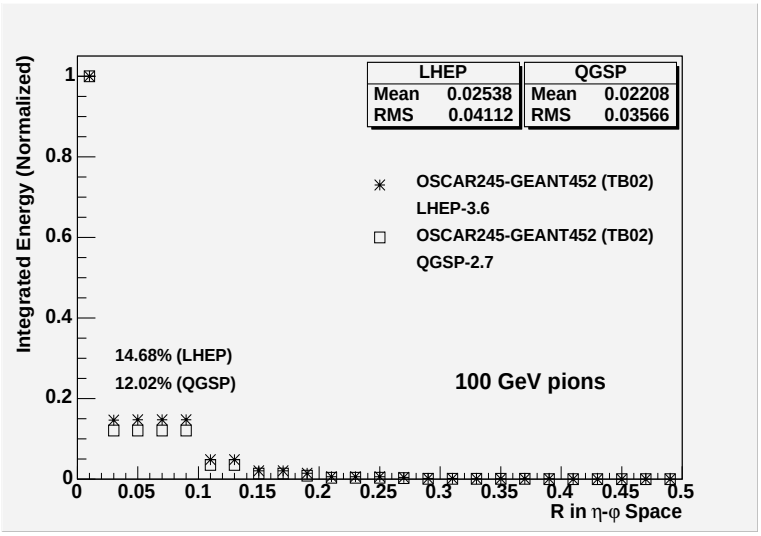

Figure 28: In the HB only configuration for pions, comparison between lateral shower profiles using both LHEP-3.6 and QGSP-2.7 physics lists in the simulation. The percent numbers in the figure refer to the fraction of energy deposited outside the central HB tower ($\eta\#$,$\phi\#$)=(9,4).

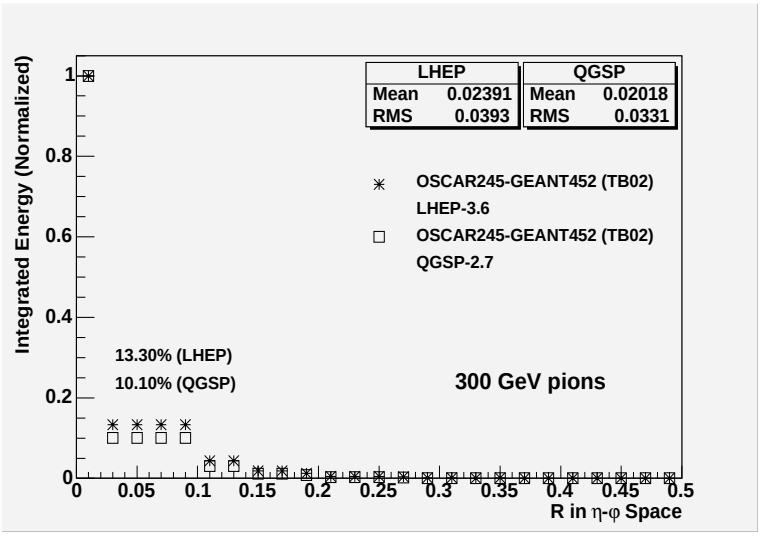

Figure 29: In the HB only configuration for pions, comparison between lateral shower profiles using both LHEP-3.6 and QGSP-2.7 physics lists in the simulation. The percent numbers in the figure refer to the fraction of energy deposited outside the central HB tower ($\eta\#$,$\phi\#$)=(9,4).

4.5 Longitudinal Shower Profiles

The longitudinal profiles of pion showers with energies of 20, 30, 50, 100, and 300 GeV were studied using the HB+HO configuration. The energy deposited in each HB layer was studied as a function of layer number: 1-17 in the HB and 18-19 in the HO. Figures 30-34 show the fraction of the shower energy measured in each layer. That is, the energy depositions in the active material (scintillator), E_{scint}, normalized by the scintillator thickness, D_{scint}, the thickness $D_{passive}$ of the passive material (brass, steel, or aluminum), a density conversion factor to express all thicknesses in brass equivalents, F_{brass}, and the total energy E_{tot} in the HB+HO system. The "Energy (Normalized to integral)" in Figs. 30-34 is, therefore:

$$\text{Energy (normalized)} = (E_{scint} \times D_{passive} \times F_{brass})/(D_{scint} \times E_{tot})$$

The scintillator thickness is 10 mm for the HO layers 18 and 19, 8 mm for the HB steel layers 1 and 17, and 4 mm for the HB brass layers 2-16. The steel plates are 7.45 cm (layer 1) and 8.9 cm thick, while the brass plates are 6 cm (layers 2-10) and 6.6 cm (layers 11-16) thick. The aluminum slab to mimic the solenoid material has a thickness of 310 mm. It is followed by 100 mm iron yoke in between the two scintillator layers, and a 195 mm HO iron block acting as tail catcher. Tower ($\eta\#$,$\phi\#$)=(9,4) points to HO Ring 1, and scintillator layer 18 is therefore absent as it is apparent in Figs. 30- 34. The means and RMS's of the longitudinal distributions are summarized in Table 2. For all pion energies, the shower predicted by the QGSP-2.7 physics list is shorter than that predicted by the LHEP-3.6 list. The fraction of the total HB+HO energy deposited in layer 19 (HO) is 1.7% (1.2%) according to LHEP-3.6 (QGSP-2.7).

Table 2: Predicted values for pion longitudinal energy profiles: mean, RMS, energy fraction deposited in the HO for pions with energies between 20 and 300 Gev.

Energy (GeV)	Physics List	Mean	RMS
20	LHEP-3.6	5.27	3.45
20	QGSP-2.7	5.26	3.39
30	LHEP-3.6	5.56	3.58
30	QGSP-2.7	5.50	3.54
50	LHEP-3.6	6.12	3.76
50	QGSP-2.7	5.84	3.65
100	LHEP-3.6	6.95	4.02
100	QGSP-2.7	6.23	3.80
300	LHEP-3.6	7.45	4.18
300	QGSP-2.7	6.84	3.99

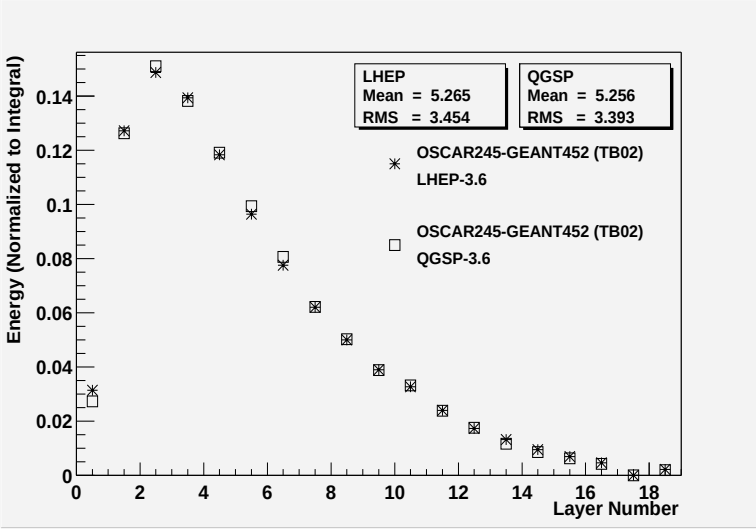

Figure 30: In the HB+HO configuration for 20 GeV pions, comparison between longitudinal shower profiles using both LHEP-3.6 and QGSP-2.7 physics lists in the simulation. The fraction of energy in each bin (or layer) is normalized to the total energy deposited in the HB+HO. The fraction of energy is also normalized by the scintillator thickness and to brass.

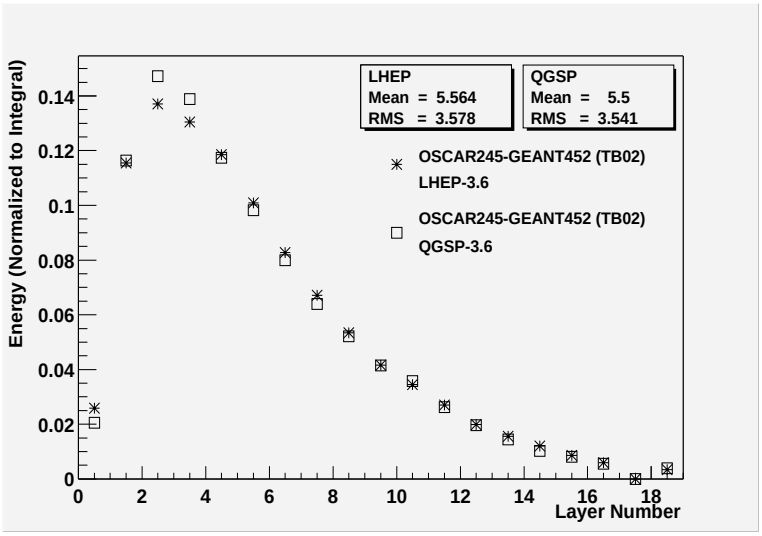

Figure 31: In the HB+HO configuration for 30 GeV pions, comparison between longitudinal shower profiles using both LHEP-3.6 and QGSP-2.7 physics lists in the simulation. The fraction of energy in each bin (or layer) is normalized to the total energy deposited in the HB+HO. The fraction of energy is also normalized by the scintillator thickness and to brass.

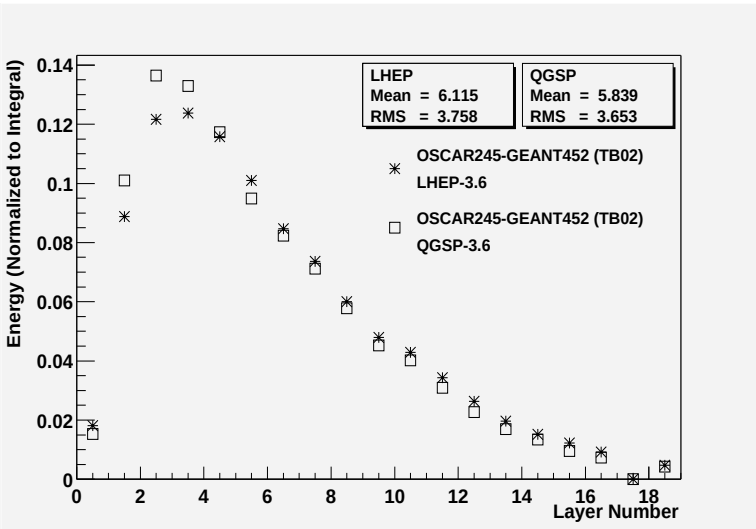

Figure 32: In the HB+HO configuration for 50 GeV pions, comparison between longitudinal shower profiles using both LHEP-3.6 and QGSP-2.7 physics lists in the simulation. The fraction of energy in each bin (or layer) is normalized to the total energy deposited in the HB+HO. The fraction of energy is also normalized by the scintillator thickness and to brass.

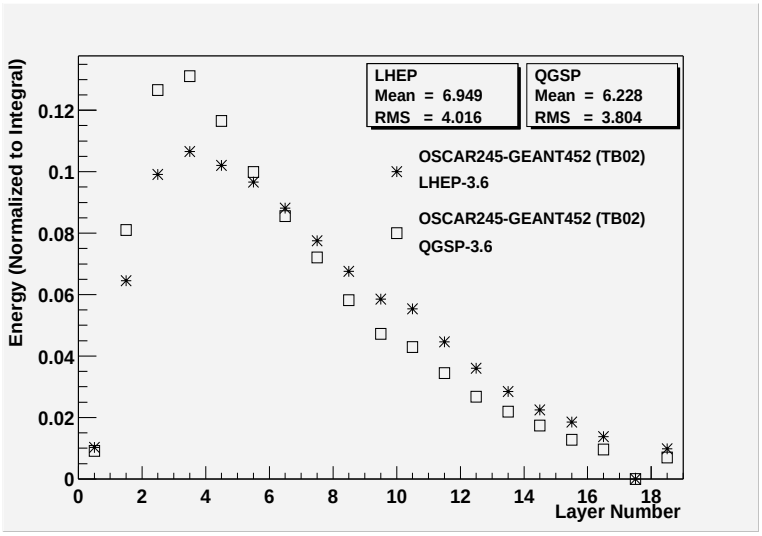

Figure 33: In the HB+HO configuration for 100 GeV pions, comparison between longitudinal shower profiles using both LHEP-3.6 and QGSP-2.7 physics lists in the simulation. The fraction of energy in each bin (or layer) is normalized to the total energy deposited in the HB+HO. The fraction of energy is also normalized by the scintillator thickness and to brass.

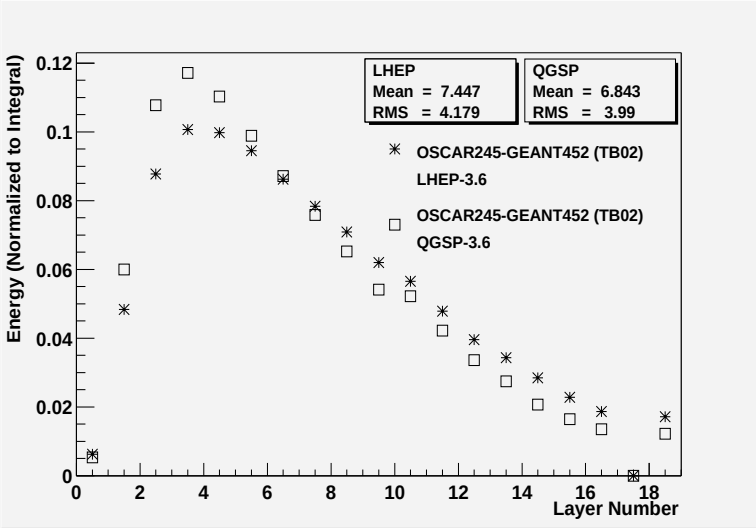

Figure 34: In the HB+HO configuration for 300 GeV pions, comparison between longitudinal shower profiles using both LHEP-3.6 and QGSP-2.7 physics lists in the simulation. The fraction of energy in each bin (or layer) is normalized to the total energy deposited in the HB+HO. The fraction of energy is also normalized by the scintillator thickness and to brass.

5 On How the HCAL Simulation Accuracy may Affect CMS Results

Monte Carlo simulations, both at the generator and the detector level, are one of the main tools for data analysis. A few examples dependent on jet and $\not\!\!E_T$ measurements, mostly based on the Tevatron (DØ) experience [13], are presented in this section to illustrate on the importance of simulation quality on the accuracy of data measurements. This will be a qualitative discussion, since a significant amount of work is needed to make a quantitative evaluation of the impact of simulation accuracy on individual measurements of interest for the CMS experiment.

At the LHC, the *Higgs Boson* would be produced in association with jets and/or would decay into jets or $\not\!\!E_T$. Typically, the tuning of the search analysis code, i.e. signal-to-background maximization in a mass window, depend significantly on the Monte Carlo to represent accurately the signal and background distributions: p_T, η, $\not\!\!E_T$.

Accurate measurements of *Jet Cross Sections* are among the most basic tests of QCD and are also essential for the understanding of QCD backgrounds in precision measurements of the properties of the top quark and the W boson, as well as in the search of the Higgs boson and new phenomena. The *Dijet Mass Cross Section* and *Dijet Mass* angular distributions may be used since day one at CMS to search for new particles such us axigluons, colorons, W'/Z' decaying to excited quarks. Quark substructure would be reveled as an excess of high p_T jet events in the most central pseudorapidity region. In all cases, an excellent understanding of jet energy scale (JES) and resolution effects is crucial, given the steeply falling nature of the jet energy spectrum. Since the jet cross section depends on E_T as E_T^{-n}, with n >5, resolution smearing effects are large. In addition, a 1% uncertainty in the JES translates into a cross section uncertainty greater than $n\%$. In general, the measurements mentioned above depend significantly on the jet algorithm choice, and the associated reconstruction efficiency, position, energy scale and resolution effects. The use of detector simulations to understand jet systematics is discussed in the next two sections.

5.1 Jet Attributes

It is important to minimize theoretical and experimental difficulties when defining jet reconstruction algorithms. According to Ref. [14], the attributes of the ideal algorithm are:

1. *Fully Specified:* The jet reconstruction process, the jet kinematic variables and corrections should be clearly and completely defined: pre-clustering, merging, splitting.
2. *Theoretically Well Behaved:* The algorithm should be infrared and collinear safe.
3. *Detector Independence:* There should be no dependence on cell type, numbers, or size.
4. *Order Independence:* The algorithm should behave equally at the parton, particle, and detector levels

Experimentally, it is desirable for an algorithm to minimize resolution smearing and angle biases, to be stable with respect to multiple hard scatterings, and to maximize reconstruction efficiency and calibration accuracy. These attributes may be achieved by tuning the jet algorithm parameters and thresholds using a Monte Carlo simulation. Even for high energy jets, a good representation of the single hadron energy response and resolution over a wide range of particle momenta is essential given the large number of low energy particles composing the jet, the underlying event, and the extra pp interactions.

Jet Reconstruction Efficiency can only be derived directly and accurately from a Monte Carlo simulation. Samples of collider γ-jet and $Z(e^+e^-, \mu^+\mu^-)$+jets data have been used at the Tevatron (DØ) with limited success, to estimate the jet reconstruction efficiency from the number of photon/Z events without any recoiling jet. This data based method is limited by the need to associate a photon/Z with a jet by means of a $\Delta\phi$ cut. In addition, light quark jets are the dominant type in γ-jet events, while gluon-jet or b-jet efficiencies are needed in many analyses. An alternate method used at DØ is based on the E_T distributions of seed towers, but it is also affected by a number of sources of systematic uncertainty such as by trigger biases, and multiple interactions.

Jet Quality Cut Efficiencies may be derived from data by applying to the sample an independent cut, very efficient removing background even if the efficiency for signal is very low. The efficiency of the quality cuts may then be studied straight forwardly from this “pure” sample. The problem with this approach is to find the independent cut which removes all background without biasing the sample and reducing statistics too much. Again, a Monte Carlo simulation which resembles the data is the only way to derive accurate efficiencies for all jet types in the whole kinematic range.

Jet Energy Resolutions were derived at DØ using a complex data based dijet (γ-jet) balance method. As in every data based method, uncertainties become significant at the edges of phase space where statistics are low. In addition, these resolutions are only accurate for gluon jets (the dominant type) and are affected by growing systematic uncertainties below 30 GeV.

Position (angular) Biases and Resolutions are extracted from Monte Carlo samples at DØ . It is difficult to think of a data based method that allows to circumvent the use of the true (η,ϕ) position.

5.2 The Jet Energy Scale

This section contains a few examples on how the detector simulations affected the derivation of the jet energy scale correction at DØ . To first order, the Run I DØ JES correction was derived from collider data provided by the calorimeters (Uranium, liquid Argon). The lack of a central magnetic field forced DØ to set aside the most obvious method to derive the JES by tuning a Monte Carlo simulation with low energy pion momentum measurements provided by a central tracking system. Instead, DØ faced the intellectual challenge of developing complex data and physics based methods [9] prescindent, at least to first order, of detector simulations.

The "true" particle level jet energy, E_{jet}^{ptcl}, was obtained at DØ with the formula:

$$E_{jet}^{ptcl} = \frac{E_{jet}^{meas} - O}{R_{jet} S_{cone}} \ ,$$

where E_{jet}^{meas} is the jet energy reconstructed at the calorimeter level, and O is an offset term accounting for the contributions of the underlying event (u.e.), multiple hard interactions, pile-up, and noise-zero suppression effects. The offset was measured from a combination of Min-Bias (a hard collision) and Zero-Bias (a crossing without any other requirement) samples. The calorimeter response to jets, R_{jet}, was measured from γ-jet and jet-jet samples using the missing p_T fraction method (MPF), based on $\not\!\!E_T$, $E_{T\gamma}$, and η_{jet}. The MPF method for obtaining R_{jet} is radically different from the alternate "photon-jet balance" method for extracting a global correction factor to the parton level energy. The showering correction, S_{cone} accounts for the fraction of the true particle jet energy leaked outside the cone limits due to the width of the shower developed in the calorimeter as the particles interacted with its material.

The final Run I jet calibration results were very competitive: 1.5% (2.3%) at 70 GeV (400 GeV) in the range $|\eta| < 0.7$. DØ published the most precise jet measurements from a hadron collider to this date, but the price in terms of time and man power was large, and there were still some uncomfortable limitations imposed by the detector simulation performance, which should be avoided in CMS to achieve the accuracy goals. Examples on how detector simulations were used directly or indirectly in many pieces of the Run I DØ JES correction are given below, and the implications discussed.

5.2.1 High Energy Response

Since the energy reach of the photons with recoiling jets in the central calorimeter (CC), $|\eta| < 0.7$, was <120 GeV in Run I, DØ used a sample with jets in the end calorimeters (EC) to extend the reach of the CC response measurement. This technique was applied after verifying that the energy dependence of the response to jets in the CC and the EC's differed only in an energy independent scale factor. For the CC and the EC's, and to avoid a jet resolution bias, R_{jet} was measured as a function of $E' = E_{T\gamma}\cosh(\eta_{jet})$ and then E' mapped to the mean E_{jet} associated with each E' bin. After including the CC and the normalized EC data points in the same plot, as shown in Fig. 35, the CC response was obtained from a fit to the data measurement. A problem arose due to the fact that the fit was not constrained beyond the 300 GeV reach of the data. The possibility of using a Geant3 detector simulation at high energies to reduce the JES uncertainty in the region beyond the reach of the γ-jet data was put aside given the discrepancy between the simulated and the measured R_{jet} in the 20-300 GeV range. Possible reasons for this discrepancy are: the modeling of the low energy pion response, the tuning of the relative sampling weights associated with calorimeter layers, the limitations imposed to calorimeter shower development to reduce computing time. Figure 36 shows a comparison between R_{jet} derived from DØ data and Monte Carlo (Geant3). The Monte Carlo response flattens out more rapidly than data and is nearly constant above 150 GeV.

The method used at DØ to constrain the response fit at high energies was based on the use of particle level generated jets convoluted with single particle test beam data to simulate the detector. The energy of each electron and hadron of a jet was scaled with the single particle test beam response functions shown in Fig. 35. Since there was no

data below 2 GeV, two extreme assumptions were made: (a) electron and pion response functions extrapolated, (c) response functions fixed. Contrary to the Geant3 simulation, the test beam based detector simulation model (b) gives an R_{jet} in excellent agreement with the R_{jet} derived from data. As shown in Fig. 35, a Monte Carlo point at 500 GeV was calculated as the average between the R_{jet} values given by the two solid lines, representing the extreme models (a) and (c). This approach is valid given the fact that the energy dependence, or shape, of the R_{jet} curve at high energy is independent of the model selected and in agreement with the R_{jet} measured in data. Figure 36 also illustrates how the addition of the Monte Carlo point constrains the $R_{jet}(E) = a + b\ln E + c\,(\ln E)^2$ fit at high energies allowing a significant reduction on the response uncertainty.

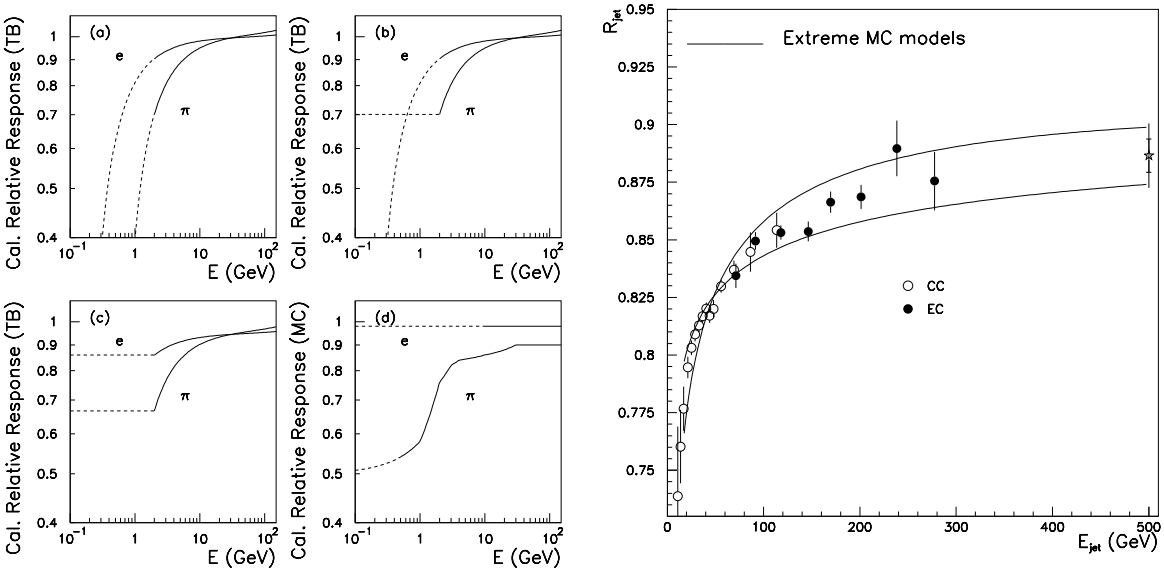

Figure 35: Left: Single particle responses for electrons and pions from DØ test beam data. Right: Jet energy response determined using the missing $\not\!\!E_T$ projection fraction method (circles) compared with the same quantity derived from Monte Carlo events and test beam single particle response (solid lines).

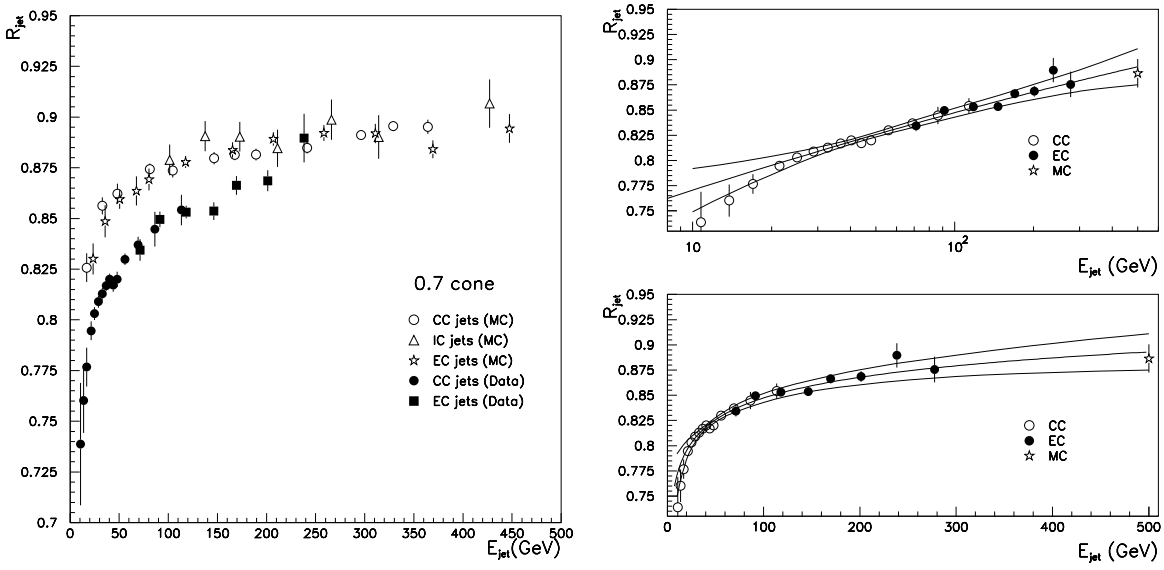

Figure 36: Left: Comparison between R_{jet} derived from DØ data and Monte Carlo (Geant3). Right: Fit to DØ R_{jet} versus E_{jet}, from CC and EC data (circles), and Monte Carlo (star).

5.2.2 Energy Leakage

The effect of energy leakage is, in principle, accounted by the MPF method. A residual mis-calibration due to leakage exists, however, because the CC response above ∼100 GeV is extracted from EC information. While the depth of the CC is $\sim 7.2\lambda_{INT}$, the thickness of the EC is $\sim 11\lambda_{INT}$ and part of the leakage correction is missed.

This residual effect was evaluated at DØ using a toy simulation based on experimental data. For the NuTeV calorimeter (stainless steel and scintillator), Fig. 37 shows the fraction of the energy of incident pions deposited beyond a certain calorimeter depths as a function of that depth in units of interaction length, λ_{INT}. The energy containment of jets at DØ was modeled using a Monte Carlo to generate jets and then the information in Fig. 37 to calculate the total energy leaked beyond the limits of the CC by all particles in the jet. Figure 37 contains the results of this study, that is the fraction of the leakage effect missed by MPF due to the use of the EC, 0.5%. A Monte Carlo simulation with a good representation of the longitudinal shower profiles for pions would be the ideal alternative to the complex method used at DØ . It would allow to study straight forwardly the jet containment as a function of pseudorapidity considering all details of the detector geometry and thickness.

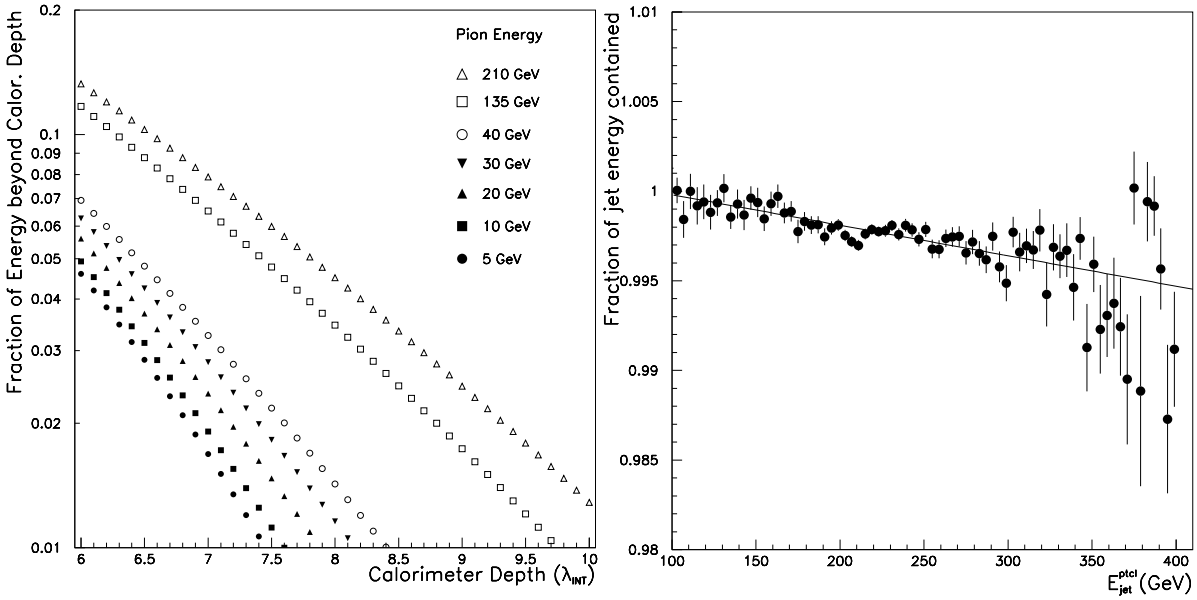

Figure 37: Left: Fraction of the pion energy escaping from the NuTeV calorimeter as a function of depth in units of interaction lengths. Right: Fraction of the jet energy contained within the DØ central calorimeter as a function of jet energy. The data are normalized to unity at 100 GeV to evaluate only the effect of using the thicker EC to derive the CC response.

5.2.3 Calorimeter Showering

At the end of Run I, DØ re-evaluated the showering correction to reduce the large uncertainties in the forward η regions [16]. This new approach was entirely Monte Carlo based and consisted of "following" each particle in the jet through the calorimeter and determining the net amount of energy leaked outside the jet cone by particles which were inside the particle level cone. The method depends critically on the simulation to model accurately the transverse shower shape of hadrons. Relevant only in the non-central regions (η >0.5), the Monte Carlo based DØ showering correction contributes a systematic uncertainty greater than 2% to the total energy scale error, coming precisely from the discrepancy between data and Monte Carlo transverse shower shapes.

6 Conclusion

Physics validation studies of Geant4 using physics lists LHEP-3.6 and QGSP-2.7, and based on HCAL test beam taken in 2002 were presented in this note. Pion energy resolution and response linearity as a function of incident energy are in good agreement with data within the large systematics uncertainties in the data measurement. Below 30 GeV, the data uncertainties are too large to provide information about deviations of the Monte Carlo model with respect to the measurements. Transverse and longitudinal shower profiles were also studied in the Monte Carlo, but no test beam 2002 data was available for comparison. The low energy pion program, E=2-9 GeV, and the transverse and longitudinal studies scheduled during the 2004 HCAL test beam experiment will be critical to understand the Geant4 physics models to the level of accuracy needed to satisfy the demands of the CMS physics program. Due to the larger center-of-mass energy of the *pp* system and the higher instantaneous luminosity, CMS

will have more physics "handles" than the experiments at the Tevatron to anchor the absolute jet energy scale to the parton level, i.e. large quantities of $Z \to b\overline{b}$, Z+jets. The need of corrections at different levels, parton and particle, for different type of jets (b, light, and gluon) in a wide p_T and η range calls, however, for an accurate detector simulation. There are a few differences between the DØ and the CMS calorimeters: non-compensation produce large non-Gaussian tails in the pion (and jet) energy distributions, the large center-of-mass energy extends the reach of the jet spectrum to the TeV range with jets containing very energetic pions penetrating deep into and beyond the calorimeter limits, the large magnetic field makes low energy charged particles to curl around and jets to become wider. These characteristics and the poor $\not\!\!E_T$ resolution impose the need to validate and improve the Tevatron methods of jet calibration when applied to CMS. One possible path is to develop an evolved version of the jet calibration technique "a la CDF", based on the generation of Monte Carlo events, a Geant4 simulation (CDF used a pre-Geant3 custom tool), and the tuning of the charge particle hadron response with energy measurements of isolated low energy tracks. To reduce the total uncertainty below the $\sim 3\%$ achieved by CDF will be a challenge. Whatever method applied, the jet and $\not\!\!E_T$ calibration will rely heavily on the accuracy of both the generators and the detector simulations.

7 Acknowledgements

I would like to thank Sunanda Banerjee for transmiting to me his HCAL simulation expertise, in particular everything related to the OSCAR simulation framework. The `HcalTB02` package is based on software he wrote for the HCAL 1999 test beam experiment. I am also grateful to a number of people who helped me with calorimeter hardware, software, test beam, and in general technical questions: S. Abdullin, P. Arce, P. De Barbaro, A. De Roeck, G. Eulisse, S. Kunori, D. Lazic, M. Liendl, M. Stavrianakou. In general, I thank the CMS HCAL, simulation, and JetMET groups.

References

[1] HTTP://CMSDOC.CERN.CH/OSCAR,

[2] S. Agostinelli et al., Nucl. Instrum. and Methods **A506**, 250 (2003).

[3] **CMS Note 2004/xxx**, V. Daniel Elvira, "CMS HCAL Test Beam 2002 Experiment: Pion Energy Response and Resolution in the HB"

[4] "The Compact Muon Solenoid Technical Proposal", The CMS Collaboration. CERN/LHCC 94-38, 1994.

[5] **CMS Note 1999/063.**, S. Banerjee, "Performance of Hadron Calorimeter with and without HO".

[6] HTTP://WWW.SGI.COM/SOFTWARE/OPENGL/OVERVIEW.HTML

[7] **CMS Note 2002/057.**, M. Imboden *et al.,* "Calibration and Performance of Lead Tungstate Electromagnetic Calorimeter for HCAL Testbeam 2002".

[8] C. Fabjan, R. Wigmans, Rep. Prog. Phys. 52 (1989).

[9] B. Abbott *et al.* (DØ Collaboration), Nucl. Instrum. and Methods **A424**, 352 (1999).

[10] **CMS Note 2000/003.**, V. V. Abramov *et al.*, "Studies of the Response of the Prototype CMS Hadron Calorimeter, Including Magnetic Field Effects, to Pion, Electron, and Muon Beams".

[11] HTTP://CMSDOC.CERN.CH/CMSIM/CMSIM.HTML,

[12] Private communication with Salavat Abduline.

[13] B. Abbott *et al.* (DØ Collaboration), Phys. Rev. **D64**, 32003, 2001.

[14] **hep-ex/0005012**, G. Blazey *et al.*, "Run II Jet Physics".

[15] B. Abbott *et al.* (DØ Collaboration), Nucl. Instrum. and Methods **A424**, 352-394 (1999).

[16] **FERMILAB-Pub 99/264-E** A. Goussiou (DØ Collaboration), "New Showering Correction for the Jet Energy Scale at DØ ".